Original Article

Crystal plasticity finite element modeling of grain size and morphology effects on yield strength and extreme value fatigue response

Aaditya Lakshmanan [a], Mohammadreza Yaghoobi [b,*],
Krzysztof S. Stopka [c], Veera Sundararaghavan [a]

[a] Department of Aerospace Engineering, University of Michigan, Ann Arbor MI 48109, USA
[b] Department of Materials Science and Engineering, University of Michigan, Ann Arbor, MI 48105, USA
[c] George W. Woodruff School of Mechanical Engineering, Georgia Institute of Technology, Atlanta, GA 30332, USA

ABSTRACT

A computational framework is presented to include the effects of grain size and morphology in the crystal plasticity finite element (CPFE) method for simulations of polycrystals. The developed framework is used to investigate the effects of grain size and morphology on the yield strength and extreme value fatigue response using a new grain-level length scale. Each grain is approximated by a best-fit ellipsoid, whose information is used to modify the slip resistances based on a Hall-Petch type relation extended to each slip system. The grain-level length scale is computed for each slip system using a shape factor proposed in an earlier work based on discrete dislocation dynamics simulations. This is incorporated into a rate-dependent CPFE model with kinematic and isotropic hardening within the PRISMS-Plasticity open-source software. CPFE simulations are conducted on Al 7075-T6 microstructure models with different textures, grain sizes, and grain morphologies which relate qualitative trends in yield strength to a parameter constructed from the power-law flow rule. Incorporating grain morphology in the model reveals a notable influence on the computed extreme value fatigue response which may be critical in simulations of polycrystalline microstructure models with significant grain morphology anisotropy, for instance in components produced by large deformation rolling or additive manufacturing. The developed framework is available to the community as part of the open-source software PRISMS-Plasticity and PRISMS-Toolbox.

1. Introduction

Effects of grain size and morphology on the mechanical properties of polycrystalline metals and alloys have been one of the most vital and challenging topics in material science and engineering. Grain size modification is one of the conventional metallurgical procedures to enhance the mechanical properties of alloys and metals. Hall [1] was one of the pioneers to study grain size effects in mild steel where an enhancement in yield strength was observed with a decrease

in grain size, and a linear relationship between the yield strength and the inverse square-root of grain size was proposed. Hall [1] justified the strength enhancement using the pile-up theory presented by Eshelby et al. [2]. Petch [3] proposed a similar relationship between the cleavage strength and grain size in iron and mild steel. Accordingly, an increase in the strength of materials by decreasing the grain size is commonly termed as the Hall-Petch effect. Since then, various experiments have been conducted on different alloy systems to investigate the Hall-Petch effect, which have been reviewed and summarized in Cordero et al. [4] and Voyiadjis and Yaghoobi [5]. The grain size effect has been addressed at different length scales using various computational frameworks, e.g., atomistic modeling [5–16], discrete dislocation dynamics [5,17–21], crystal plasticity [5,22–31] and continuum plasticity [5,32–35]. These simulation methodologies have their own strengths and limitations. Among these, crystal plasticity has proven to be a useful tool for modeling the mechanical behavior of polycrystalline metals and alloys considering microstructure features and common plastic deformation modes such as crystallographic slip and twinning.

In modeling grain size effects in crystal plasticity, the enhanced hardening due to dislocation pile-up can be modeled using strain gradient crystal plasticity [5,18,22–25]. These models can successfully capture the effect of grain size using a robust thermodynamically consistent framework. However, there are challenges with using strain gradient models to capture the grain size effect. The first challenge is that strain gradient models introduce more internal variables and subsequently more model parameters which require many experiments to adequately calibrate. Secondly, the available strain gradient models in the literature do not naturally consider the morphological features of grains. An alternative to strain gradient models was presented by Haouala et al. [31] in which the evolution of the critical resolved shear stress of each slip system is governed by its corresponding dislocation density. The effect of grain size is then reflected in the dislocation density evolution depending on the distance of material point from the grain boundary. This method can be further simplified by homogenizing the grain size effect in each grain and then relating the critical resolved shear stress to the grain size [26,29,36]. This scheme enables the simulation of very large volumes of material using crystal plasticity models, which is an essential part of many integrated computational materials engineering (ICME) frameworks. Fromm et al. [37] introduced a new grain size and orientation distribution function (GSODF) to couple the effect of texture and grain size within a viscoplastic Taylor-like framework. They observed that the interaction between texture and grain size may lead to large anisotropy in yield strength. Their method does not, however, consider the effects of grain morphology and therefore cannot adequately model microstructures with elongated grains, such as those that arise due to rolling or additive manufacturing.

Unlike the effect of grain size on the response of polycrystalline materials, which has been widely investigated, the effect of grain morphology has not been completely unraveled. A few studies have addressed the effect of grain morphology on the response of polycrystals [38–40]. Bunge et al. [38]

combined the Hall–Petch relationship with the Taylor model [41] to capture the effect of grain morphology. They approximated each grain as an ellipsoid and obtained the grain size along each slip direction using the specific line that passes through the center of the ellipsoid. However, they did not consider the evolution of texture. Delannay et al. [42] investigated the plastic anisotropy of textured polycrystalline aggregates resulting from three micro-macro averaging schemes—a crystal plasticity based finite element model, the viscoplastic self-consistent (VPSC) scheme, and a "multisite" model based on a simplified treatment of the interaction of adjacent grains. Delannay and Barnett [43] proposed closed-form expressions of the average backstress developed inside grains with spheroidal shapes which are introduced in the crystal plasticity hardening law. This model reproduced the high plastic anisotropy of electro-deposited pure iron with a strong γ-fiber and a refined columnar grain structure. However, they did not consider the general case of ellipsoidal grains and the focus of their study was not directed towards the dependence of Hall-Petch slope on grain morphology. Sun and Sundararaghavan [29] addressed the effect of grain morphology by incorporating the idea proposed by Fromm et al. [37] along with the ellipsoid approximation of Bunge et al. [38]. They presented a very efficient statistical approach that can evolve the GSODF during deformation. Although the statistical polycrystal scheme presented by Sun and Sundararaghavan [29] is very robust and efficient to capture the homogenized response, it cannot resolve local stress and strain fields within grains.

More precisely, all the proposed methods to address grain morphology within a crystal plasticity framework [29,38–40] are homogenized methods, such as Taylor-type models, and cannot resolve local variations in the stress and strain fields. The crystal plasticity finite element (CPFE) framework, however, can handle these issues since it benefits from all features of conventional finite element methods. The current study presents a CPFE framework which considers the effects of grain size and morphology specifically designed for large scale simulations. In this framework, grains are modeled as ellipsoids following the idea of Bunge et al. [38] to capture the coupling effects between grain size and morphology, while allowing prediction of local fields unlike the previously described mean-field methodologies. The use of CPFE allows improved modeling of internal equilibrium of forces exerted by grains of different shapes and sizes.

In the current work, a rate-dependent model including both kinematic and isotropic hardening is implemented into the open-source CPFE software, PRISMS-Plasticity [44–48]. A new grain-level length scale is integrated into the CPFE framework to capture the effects of grain size and morphology. The length scale definition is based on results reported by Jiang et al. [21] which incorporated discrete dislocation dynamics simulation to investigate the effects of grain size, orientation, and morphology on flow stress. Each grain is approximated by its best-fit ellipsoid to obtain the grain-level length scale, which inherently includes grain morphology effects. This measure of grain size is used to modify the slip resistances, hence incorporating the effects of grain size and morphology into the crystal plasticity formulation. The response of Al 7075-T6 polycrystalline microstructure models with different crystallographic textures, grain sizes, and grain morphologies are

then investigated to demonstrate the capability of the developed framework. The effects of grain size and morphology on yield strength are first investigated. Accordingly, the Hall-Petch slopes are obtained for different textures and grain morphologies. The local micromechanical and extreme value fatigue response is then investigated for samples with a similar average grain size but different grain morphologies to highlight the importance of the latter. The grain morphology may have important implications on the extreme value fatigue response that is often evaluated using crystal plasticity models [49].

2.   Crystal plasticity constitutive model

The primary kinematic ingredient of the constitutive model for an elasto-plastic single crystal is the deformation gradient tensor F, which is the tangent map of a smooth deformation mapping that associates the position of material points in the reference configuration to their corresponding position in the deformed configuration. A multiplicative decomposition of the deformation gradient into elastic and plastic parts is considered here as follows [50,51]:

$$F = F^e F^p \tag{1}$$

where F^p captures the homogenized distortion of the body as a consequence of crystallographic slip due to dislocation motion on specific slip systems and maps infinitesimal material fibers in the reference configuration to their counterparts in the intermediate configuration. F^e is the elastic part of the deformation gradient tensor which encodes elastic stretch and rotation of the lattice and maps the intermediate configuration to the deformed configuration.

The plastic part of the velocity gradient in the intermediate configuration is related to the underlying crystallography through the plastic kinematic equation

$$L^p := \dot{F}^p F^{p-1} = \sum_{\alpha=1}^{n_s} \dot{\gamma}^\alpha S_0^\alpha = \sum_{\alpha=1}^{n_s} \dot{\gamma}^\alpha m_0^\alpha \otimes n_0^\alpha \tag{2}$$

where $\dot{F}^p$ denotes the material time derivative of F^p, n_s is the total number of slip systems and $\dot{\gamma}^\alpha$ is the shear rate on slip system α ($\alpha \in \{1, 2, ..., n_s\}$. m_0^α and n_0^α are unit vectors associated with the slip direction and slip plane normal, respectively, for slip system α in the intermediate configuration. S_0^α is the Schmid tensor corresponding to slip system α defined as the tensor product of m_0^α and n_0^α. Eq. (2) physically represents the shearing of the body from plastic flow on plane n_0^α along direction m_0^α.

In the present case, we resort to a flow rule where the shearing rate on slip system α is explicitly related to the resolved shear stress, backstress and slip resistance on that slip system. Following [52] and modifying it to include the backstress contribution, we assume a flow rule of the power law type as follows

$$\dot{\gamma}^\alpha = \dot{\gamma}^0 \left(\frac{\|\tau^\alpha - \chi^\alpha\|}{s^\alpha} \right)^m \text{sign}(\tau^\alpha - \chi^\alpha) \tag{3}$$

where $\dot{\gamma}^0$ is the reference shearing rate and m is the strain-rate sensitivity exponent, both assumed to be identical for all slip systems. τ^α, χ^α and s^α are the resolved shear stress, the

backstress and the slip resistance, respectively, on slip system α. sign(·) denotes the signum function. Eq. (3) is one possible regularization adopted to avert the under-determined system of equations arising in Eq. (2) where there are 8 independent components of L^p while $n_s > 8$ for the crystal structures of interest. The backstress is included to account for kinematic hardening that manifests as the Bauschinger Effect, while the slip system resistance accounts for the isotropic hardening of the material. Specific evolutionary equations for the backstress and the slip system resistance are discussed later.

The resolved shear stress is expressed in terms of the second Piola-Kirchoff stress in the intermediate configuration, T, as follows

$$\tau^\alpha = \left(F^{eT} F^e T \right) : S_0^\alpha \tag{4}$$

where the '∶' denotes the scalar product of second-order tensors, i.e., $A : B = A_{ij} B_{ij}$. Eq. (4) is obtained by equating the continuum mechanical contribution of plastic power density to the power expended in crystallographic shearing on slip system α with shearing rate $\dot{\gamma}^\alpha$ and resolved shear stress τ^α [53]. Following [54], we further approximate the resolved shear stress by ignoring the effects of elastic stretching, which are not significant for the levels of deformation considered. Then we have

$$\tau^\alpha \approx T : S_0^\alpha \tag{5}$$

The elastic constitutive equation is motivated from a generalized version of standard Hooke's law where a linear relation relationship is prescribed between T and the Green—Lagrange elastic strain measure (elastic power conjugate to T) as follows

$$T = \mathcal{L} \cdot E^e = \frac{1}{2} \mathcal{L} \cdot (F^{eT} F^e - I) \tag{6}$$

where $\mathcal{L}$ denotes the fourth-order material stiffness tensor which is positive-definite and exhibits both major and minor symmetries typical of hyperelastic constitutive laws when symmetric tensors are involved. The '·' denotes the product of a fourth-order and second-order tensor furnishing a second-order tensor, i.e., $A = \mathcal{L} \cdot B \Rightarrow A_{ij} = \mathcal{L}_{ijkl} B_{kl}$. T is related to the first Piola-Kirchoff stress in the reference configuration and the Cauchy stress as follows:

$$T = F^{e-1} P F^{T} F^{e-T} = \det(F^e) F^{e-1} \sigma F^{e-T} \tag{7}$$

The dislocation-induced long range stresses for each slip system result in the back stress, which is modeled here using a two-term phenomenological formulation developed by Ohno-Wang [55]. The model was further modified by McDowell [56] to simulate ratcheting behavior in rail steels. On every slip system α, two independent back stress components, i.e., χ_1^α and χ_2^α, are defined which evolve as follows

$$\dot{\chi}_i^\alpha = h_i \dot{\gamma}^\alpha - r_i \left(\frac{\chi_i^\alpha}{b_i} \right)^{m_i} \chi_i^\alpha \dot{\gamma}^\alpha \; ; (i = 1, 2)$$

$$\dot{\chi}^\alpha = \sum_{i=1}^{2} \dot{\chi}_i^\alpha, \; \chi_i^\alpha(t = 0) \; = \; 0 \; ; (i = 1, 2) \tag{8}$$

where h_i, r_i, b_i and m_i are the constant model parameters with $b_i = h_i/r_i$ which denotes the saturation value of the backstress.

The evolution of slip resistance is prescribed based on Kalidindi et al. [54] as follows

$$\dot{s}^\alpha = \sum_{\alpha=1}^{n_s} q_{\alpha\beta} h_0 \left(1 - \frac{s^\beta}{s^s}\right)^a \|\dot{\gamma}^\beta\| \; ; \; s^\alpha(0) = s_0^\alpha \tag{9}$$

$$q_{\alpha\beta} = q + (1-q)\tilde{\delta}_{\alpha\beta}$$
$$\tilde{\delta}_{\alpha\beta} = \begin{cases} 1 \; ; & \alpha, \beta \text{ are coplanar} \\ 0 \; ; & \text{otherwise} \end{cases} \tag{10}$$

where $q_{\alpha\beta}$ denotes the hardening multiplier contribution to slip system α arising from slip on slip system β. h_0 is the hardening coefficient, s_s is the saturation values of the slip resistance and a is the hardening exponent. To summarize, the model presented here represents a cyclically stabilized hysteresis response and does not incorporate damage or degradation.

3. Grain size and morphology effects

The effects of grain size and morphology are incorporated in the model by including a grain-level length scale and modifying the initial slip resistance using this length scale. Accordingly, the slip resistance includes two contributions; one independent of the grain size and morphology and the other dependent on both grain size and morphology, defined as

$$s_0^\alpha = s_{SI}^\alpha + s_{SD}^\alpha \tag{11}$$

where s_{SI}^α and s_{SD}^α are the size independent and dependent contributions to initial slip resistance, respectively. The size dependent contribution is assumed to abide to a Hall-Petch type inverse square-root dependence on the grain size, which also depends on the slip system as follows:

$$s_{SD}^\alpha = \frac{k^\alpha}{\sqrt{d_{eff}^\alpha}} \tag{12}$$

where d_{eff}^α is an effective grain-level length scale corresponding to the slip system α. The grain-level length scale is obtained by finding the best-fit ellipsoid for each grain, which includes the semi-axes lengths and the axes Euler angles relative to the sample reference frame. The components of the slip direction m_0^α and slip plane normal n_0^α are represented relative to the principal axes frame of the best-fit ellipsoid for each slip system, which we denote by m_e^α and n_e^α respectively. Let t_e^α denote the direction lying in the slip plane perpendicular to m_e^α. Then t_e^α can be obtained via $t_e^\alpha = m_e^\alpha \times n_e^\alpha$, where ' $\times$ ' is vector cross product. The directions t_e^α and m_e^α are essential here since they signify the direction of propagation of the pure-edge and pure-screw counterparts of deformation accommodating dislocation loops on slip system α. This information is used to calculate d_{eff}^α.

The standard ellipsoid is defined here as the ellipsoid $\mathcal{E} \subseteq \mathbb{R}^3$ centered at the origin with its principal axes coinciding as the axes of the coordinate system. The surface of the standard ellipsoid can be characterized as follows:

$$f(x, y, z) = \frac{x^2}{a_1^2} + \frac{y^2}{a_2^2} + \frac{z^2}{a_3^2} - 1 = 0 \tag{13}$$

One can consider a line ℓ intersecting $\mathcal{E}$ at no less than one point, represented by its parametric form as follows:

$$p(t) = (\omega_1 + \lambda_1 t, \omega_2 + \lambda_2 t, \omega_3 + \lambda_3 t) \tag{14}$$

where $(\omega_1, \omega_2, \omega_3)$ denotes a point on ℓ and $(\lambda_1, \lambda_2, \lambda_3)$ denotes the direction cosines of ℓ. Define d_ℓ as the length of the line segment contained in ℓ lying in the interior of $\mathcal{E}$, which is referred as the line-ellipsoid intercept). Because $\mathcal{E}$ is convex, given a specific line ℓ, d_ℓ is well-defined and unique. Let Λ be the set of all lines ℓ with the same slope, rigidly displaced relative to one another and intersecting $\mathcal{E}$ in at least one point. The goal is to obtain $<d_\ell>_\Lambda$, where $<\cdot>_\Lambda$ denotes the average of the bracketed argument.

The interior of the ellipsoid is denoted by $\tilde{\mathcal{E}}$, i.e., the set of all points satisfying $f(x, y, z) < 0$. One can substitute the point $p(t)$ as defined in Eq. (14) into Eq. (13) as follows:

$$\frac{(\omega_1 + \lambda_1 t)^2}{a_1^2} + \frac{(\omega_2 + \lambda_2 t)^2}{a_2^2} + \frac{(\omega_3 + \lambda_3 t)^2}{a_3^2} - 1 = 0$$

$$\Rightarrow t^2 \underbrace{\left(\sum_{i=1}^3 \frac{\lambda_i^2}{a_i^2}\right)}_{\kappa_1} + t \underbrace{\left(\sum_{i=1}^3 \frac{2\lambda_i\omega_i}{a_i^2}\right)}_{\kappa_2} + \underbrace{\left(\sum_{i=1}^3 \frac{\omega_i^2}{a_i^2}\right) - 1}_{\kappa_3} = 0 \tag{15}$$

$$\Rightarrow \kappa_1 t^2 + \kappa_2 t + \kappa_3 = 0$$

Eq. (15) must have two distinct real roots of t_1 and t_2. Accordingly, d_ℓ can be written as follows:

$$d_\ell = \sqrt{\sum_{i=1}^3 \lambda_i^2 (t_2 - t_1)^2} = \frac{1}{\kappa_1}\sqrt{\kappa_2^2 - 4\kappa_1\kappa_3} \; ; \; \kappa_1 > 0 \tag{16}$$

The parametrization for the family of lines Λ is required to obtain $<d_\ell>_\Lambda$, and this is performed using two-parameters. One should note that obtaining $<d_\ell>_\Lambda$ requires integrating d_ℓ over the set described by the two-parameter family. A convenient parametrization choice eases the integration of d_ℓ and leads to an straightforward procedure to obtain $<d_\ell>_\Lambda$.

The first step is to identify the set $Q \subseteq \mathcal{E}$ of points such that the line ℓ with direction cosines $\lambda = (\lambda_1, \lambda_2, \lambda_3)$ passing through $q \in Q$ is a tangent to the ellipsoid. This warrants the following conditions on the point $q = (x_q, y_q, z_q)$

$$\frac{x_q^2}{a_1^2} + \frac{y_q^2}{a_2^2} + \frac{z_q^2}{a_3^2} - 1 = 0, \; \lambda \cdot \nabla f = 0 \tag{17}$$

$$\Rightarrow \frac{\lambda_1 x_q}{a_1^2} + \frac{\lambda_2 y_q}{a_2^2} + \frac{\lambda_3 z_q}{a_3^2} = 0 \tag{18}$$

At least one of the direction cosines is non-zero according to $\sum_{i=1}^3 \lambda_i^2 = 1$. Without loss of generality, one can assume $\lambda_3 \neq 0$, and Eq. (18) can be rewritten as follows:

$$z_q = \frac{-a_3^2}{\lambda_3}\left(\frac{\lambda_1 x_q}{a_1^2} + \frac{\lambda_2 y_q}{a_2^2}\right) = g(x_q, y_q) \tag{19}$$

Eq. (19) can be substituted into Eq. (17) as follows:

$$\frac{x_q^2}{a_1^2}+\frac{y_q^2}{a_2^2}+\frac{1}{a_3^2}\left(\frac{-a_3^2}{\lambda_3}\left(\frac{\lambda_1 x_q}{a_1^2}+\frac{\lambda_2 y_q}{a_2^2}\right)\right)^2-1=0$$

$$\Rightarrow\ x_q^2\cdot\underbrace{\left(\frac{1}{a_1^2}+\frac{a_3^2\lambda_1^2}{\lambda_3^2 a_1^4}\right)}_{p}+y_q^2\cdot\underbrace{\left(\frac{1}{a_2^2}+\frac{a_3^2\lambda_2^2}{\lambda_3^2 a_2^4}\right)}_{q}+x_q y_q\cdot\underbrace{\frac{2\lambda_1\lambda_2 a_3^2}{a_1^2 a_2^2\lambda_3^2}}_{2r}-1=0$$

$$\tag{20}$$

Eq. (20) represents an ellipse, which be confirmed by evaluating the conic discriminant $D=(2r)^2-4pq$ and examining its sign as follows:

$$4(r^2-pq)=4\left\{\left(\frac{\lambda_1\lambda_2 a_3^2}{a_1^2 a_2^2\lambda_3^2}\right)^2-\left(\frac{1}{a_1^2}+\frac{a_3^2\lambda_1^2}{\lambda_3^2 a_1^4}\right)\cdot\left(\frac{1}{a_2^2}+\frac{a_3^2\lambda_2^2}{\lambda_3^2 a_2^4}\right)\right\}$$

$$\le\frac{-4}{a_1^2 a_2^2}<0$$

$$\tag{21}$$

The ellipse defined by Eq. (20) is denoted by E and its interior is denoted by $\tilde{E}$.[1] For any point $(x,y)\in\tilde{E}$, one can obtain $z(x,y)$ from Eq. (19). Geometrically, the set $F:=\{(x,y,g(x,y))\}\ \forall\ (x,y)\in\tilde{E}$ represents the intersection of the plane (Eq. (18)) with $\widetilde{\mathcal{E}}$.

Any line $\ell\in\mathcal{L}$ with direction cosines λ which passes through $\widetilde{\mathcal{E}}$ must intersect $\mathcal{E}$ at exactly two points because $\mathcal{E}$ is convex. We now prove that any such line ℓ must intersect F. Note that only the portion $l=\ell\cap\tilde{E}$ is of interest because that defines d_ℓ. One can show that $l\cap F\ne\varphi$ by proving that the two intersection points of ℓ with $\mathcal{E}$, lie on opposite sides of F or equivalently of the plane defined by Eq. (18). One can define:

$$h(x,y,z)=\frac{\lambda_1 x}{a_1^2}+\frac{\lambda_2 y}{a_2^2}+\frac{\lambda_3 z}{a_3^2}\tag{22}$$

If the points of intersection of ℓ with $\mathcal{E}$ are denoted by (x_1,y_1,z_1) and (x_2,y_2,z_2), then for these two points to lie on opposite sides of the plane, it is sufficient that they satisfy the following condition:

$$h(x_1,y_1,z_1)h(x_2,y_2,z_2)<0\tag{23}$$

From Eq. (15), one can substitute the points as $(x_1,y_1,z_1)=(\omega_1+\lambda_1 t_1,\ \omega_2+\lambda_2 t_1,\ \omega_3+\lambda_3 t_1)$ and $(x_2,y_2,z_2)=(\omega_1+\lambda_1 t_2,\ \omega_2+\lambda_2 t_2,\ \omega_3+\lambda_3 t_2)$. Substituting the points in Eqs. (22) and (23) can be written as follows:

$$V=h(x_1,y_1,z_1)h(x_2,y_2,z_2)$$

$$=\left(\frac{\lambda_1 x_1}{a_1^2}+\frac{\lambda_2 y_1}{a_2^2}+\frac{\lambda_3 z_1}{a_3^2}\right)\cdot\left(\frac{\lambda_1 x_2}{a_1^2}+\frac{\lambda_2 y_2}{a_2^2}+\frac{\lambda_3 z_2}{a_3^2}\right)=\frac{-1}{4}(\kappa_2^2-4\kappa_1\kappa_3)<0$$

$$\tag{24}$$

Eqs. (22)–(24) shows that $\ell\cap F\ne\varphi$ implying that for every line $\ell\in\mathcal{L}$, there is a unique point $p\in F$ such that $p\in\ell$. Now, there is a bijection $\tilde{g}$ from F to $\mathcal{L}$ which simplifies the analysis because any admissible line ℓ can be parametrized by only a point on F. Furthermore, g is a bijection, which implies that the composition $\bar{g}=\tilde{g}\circ g$ is a bijection from $\tilde{E}$ to $\mathcal{L}$.

The parametrization for the ellipse E should be defined in the next step. The ellipse E can be defined as follows:

$$px^2+qy^2+2rxy=1\tag{25}$$

---

[1] The interior of the ellipse is defined by the set of points satisfying the equation $px^2+qy^2+2xyr-1<0$.

The major and minor axes of an ellipse are orthogonal. Furthermore, the plane, as described in Eq. (18), passes through the origin in $\mathbb{R}^3$ which implies that F contains the origin in $\mathbb{R}^3$, and consequently, E contains the origin in $\mathbb{R}^2$. In other words, the major and minor axes pass through the origin so that any such ellipse can be represented as follows:

$$(\alpha x+\beta y)^2+\gamma^2(\beta x-\alpha y)^2=1\tag{26}$$

Comparing Eqs. (25) and (26) yields:

$$\alpha^2+\gamma^2\beta^2=p\tag{27}$$

$$\beta^2+\gamma^2\alpha^2=q\tag{28}$$

$$\alpha\beta(1-\gamma^2)=r\tag{29}$$

Based on the values of r, γ, and α, three different cases may occur as follows:

Case 1: $r\ne0$

Eq. (29) can be rewritten as follows:

$$\alpha\beta=\frac{r}{1-\gamma^2}\tag{30}$$

Eqs. (27) and (28) can be rewritten as follows:

$$\alpha^2=\frac{p-q\gamma^2}{(1-\gamma^2)(1+\gamma^2)}\ ;\ \beta^2=\frac{q-p\gamma^2}{(1-\gamma^2)(1+\gamma^2)}\tag{31}$$

One can combine Eqs. (30) and (31) as follows:

$$\frac{(p-q\gamma^2)(q-p\gamma^2)}{(1+\gamma^2)^2}=r^2\tag{32}$$

$\delta:=\gamma^2$ can be defined and substituted in Eq. (32) as follows:

$$\delta^2(r^2-pq)+\delta(2r^2+p^2+q^2)+r^2-pq=0\tag{33}$$

The roots of Eq. (33) can be obtained as follows:

$$\delta_\pm=\frac{1}{2(r^2-pq)}\left((-(2r^2+p^2+q^2)\pm\sqrt{(2r^2+p^2+q^2)^2-4(r^2-pq)^2}\right)$$

$$\tag{}$$

Choice of either δ_+ or δ_- results in the same ellipse so $\delta=\delta_+$ is selected. One should note that the ellipse is invariant under the transformation $\gamma\to-\gamma$, so the positive value of γ suffices and $\gamma=\sqrt{\delta_+}$. The ellipse is invariant under the transformation $\alpha\to-\alpha$, $\beta\to-\beta$, so a positive value of α is chosen, and β is fixed accordingly (Eq. (30)). One can obtain α and β as follows:

$$\alpha=\sqrt{\frac{p-q\delta_+}{(1-\delta_+)(1+\delta_+)}},\ \beta=\frac{r}{(1-\delta_+)\alpha}\tag{34}$$

Case 2: $r=0,\ \gamma^2=1$

The left hand side of Eqs. (27) and (28) are identical which leads to $p=q$, i.e., the ellipse becomes a circle. Then α and β have only one constraint to satisfy as $\alpha^2+\beta^2=p$. For convenience, one can select $\alpha=\sqrt{p}$ and $\beta=0$.

Case 3: $r=0,\ \alpha=0$

In this case, $\beta^2 = q$. One can set $\beta = \sqrt{q}$, and accordingly set $\gamma = \sqrt{\frac{p}{q}}$.

α, β and γ can be obtained from one of the previous three cases, and E can be parametrized as follows:

$$\alpha x + \beta y = R\cos\theta \tag{35}$$

$$\gamma\beta x - \gamma\alpha y = R\sin\theta \tag{36}$$

Eqs. (35) and (36) can be combined as follows:

$$\begin{bmatrix} \alpha & \beta \\ \gamma\beta & -\gamma\alpha \end{bmatrix} \cdot \begin{bmatrix} x \\ y \end{bmatrix} = \begin{bmatrix} R\cos\theta \\ R\sin\theta \end{bmatrix} \tag{37}$$

x and y can then be obtained as follow:

$$\begin{bmatrix} x \\ y \end{bmatrix} = \frac{1}{\gamma(\alpha^2 + \beta^2)} \begin{bmatrix} \gamma\alpha & \gamma\beta \\ \beta & -\alpha \end{bmatrix} \begin{bmatrix} R\cos\theta \\ R\sin\theta \end{bmatrix} \tag{38}$$

x and y can be described as a function of R and θ as $x = X(R, \theta)$ and $y = Y(R, \theta)$. Similarly, z can be defined as $z = Z(R, \theta)$. Also, one can define $\omega_1 = X(R, \theta)$, $\omega_2 = Y(R, \theta)$, $\omega_3 = Z(R, \theta)$ so that $\kappa_2 \equiv \kappa_2(R, \theta)$ and $\kappa_3 \equiv \kappa_3(R, \theta)$.

The average value of d_ℓ, i.e., $<d_\ell>_\Lambda$, is defined as follows:

$$<d_\ell>_\Lambda = \frac{\iint_E d_\ell(x,y)dxdy}{\iint_E dxdy} \tag{39}$$

The above expression is well-defined because $d_\ell(x, y)$ is a continuous function and E is a compact set in $\mathbb{R}^2$. Changing variables of integration from x, y to R, θ enables integration over a rectangular domain. Defining $\tilde{d}_\ell(R, \theta) = d_\ell(x, y)$ results in:

$$<d_\ell>_\Lambda = \frac{\iint_E \tilde{d}_\ell(R,\theta)JdRd\theta}{\iint_E JdRd\theta} \tag{40}$$

where J is the Jacobian of the coordinate transformation (Eqs. (35) and (36)). J can be obtained as follows:

$$J = \det\left(\begin{bmatrix} \dfrac{\partial x}{\partial R} & \dfrac{\partial x}{\partial \theta} \\ \dfrac{\partial y}{\partial R} & \dfrac{\partial y}{\partial \theta} \end{bmatrix} \right)$$

$$= \frac{1}{(\gamma(\alpha^2+\beta^2))^2} \cdot \det\left(\begin{bmatrix} \gamma\alpha & \gamma\beta \\ \beta & -\alpha \end{bmatrix} \begin{bmatrix} \cos\theta & -R\sin\theta \\ \sin\theta & R\cos\theta \end{bmatrix} \right)$$

$$= \frac{R}{\gamma(\alpha^2+\beta^2)} \tag{41}$$

One can rewrite Eq. (40) using Eqs. (16) and (41) as follows:

$$<d_\ell>_\Lambda = \frac{\displaystyle\int_0^{2\pi}\int_0^1 \frac{1}{\kappa_1}\sqrt{\kappa_2^2 - 4\kappa_1\kappa_3}R\ dRd\theta}{\displaystyle\int_0^{2\pi}\int_0^1 R\ dRd\theta}$$

$$= \frac{1}{\kappa_1\pi}\int_0^{2\pi}\int_0^1 R\sqrt{\kappa_2(R,\theta)^2 - 4\kappa_1\kappa_3(R,\theta)}\ dRd\theta \tag{42}$$

Eq. (42) can be rewritten as follows:

$$<d_\ell>_\Lambda = \frac{1}{\kappa_1\pi}\int_0^{2\pi}\int_0^1 \left\{A + DR^2 + BR^2\cos^2\theta + CR^2\cos\theta\sin\theta\right\}^{\frac{1}{2}} R\ dRd\theta \tag{43}$$

The integral described in Eq. (43) can be obtained analytically by changing variable from R to $s = A + DR^2 + B(R\cos\theta)^2 + CR^2\cos\theta\sin\theta$. Accordingly, Eq. (43) can be rewritten as follows:

$$<d_\ell>_\Lambda = \frac{1}{\kappa_1\pi}\int_0^{2\pi}\int_{\sqrt{A}}^{\sqrt{M(\theta)}} \frac{\sqrt{s}}{2(M(\theta)-A)}\ dsd\theta$$

$$= \frac{1}{3\kappa_1\pi}\int_0^{2\pi} \frac{M(\theta)\sqrt{M(\theta)} - A\sqrt{A}}{M(\theta)-A}d\theta \tag{44}$$

where $M(\theta) = A + D + B\cos^2\theta + C\cos\theta\sin\theta$. Note that the quantity $M(\theta)/\kappa_1$ represents the line-ellipsoid intercept at $R = 1$, at which by construction, the line is tangent to, so that $M(\theta) = 0$; $\forall\theta \in [0, 2\pi)$. This transforms the integral to a much simpler one as follows:

$$<d_\ell>_\Lambda = \frac{1}{3\kappa_1\pi}\int_0^{2\pi} \frac{-A\sqrt{A}}{-A}d\theta = \frac{2\sqrt{A}}{3\kappa_1} \tag{45}$$

κ_1 is defined in Eq. (15), and by computing $\kappa_2(R, \theta)$ and $\kappa_3(R, \theta)$ one can derive $A = 4\kappa_1$. Accordingly, Eq. (45) can be rewritten as follows:

$$<d_\ell>_\Lambda = \frac{4}{3\sqrt{\displaystyle\sum_{i=1}^3\left(\frac{\lambda_i}{a_i}\right)^2}} \tag{46}$$

where λ_1, λ_2, λ_3 are the direction cosines of the family Λ, and a_1, a_2, a_3 are the semi-axes lengths of $\mathcal{E}$. The expression in Eq. (46) is similar to the one suggested by Bunge et al. [38] except for a multiplication factor. In the current work, the formulation is developed using the averaging operator which is different from the formulation developed by Bunge et al. [38] based on the line intercept passing through the origin of the ellipsoid. One can use Eq. (46) to obtain the effective length scales corresponding to pure-edge and pure-screw dislocations with the direction cosines of $\boldsymbol{m}_e^\alpha(m_{e,1}^\alpha, m_{e,2}^\alpha, m_{e,3}^\alpha)$ and $\boldsymbol{t}_e^\alpha(t_{e,1}^\alpha, t_{e,2}^\alpha, t_{e,3}^\alpha)$, respectively, as follows:

$$d_{m_e^\alpha} = \frac{4}{3\sqrt{\displaystyle\sum_{i=1}^3\left(\frac{m_{e,i}^\alpha}{a_i}\right)^2}}, d_{t_e^\alpha} = \frac{4}{3\sqrt{\displaystyle\sum_{i=1}^3\left(\frac{t_{e,i}^\alpha}{a_i}\right)^2}} \tag{47}$$

Jiang et al. [21] conducted a set of discrete dislocation dynamics simulations and proposed a shape factor to account for the grain size and morphology on the flow stress. The proposed length scale is used here to obtain the slip system-level length scale. Accordingly, the effective length scale for slip system α can be obtained as follows:

$$d_{\text{eff}}^\alpha = \left(\frac{4S^\alpha}{C^\alpha}\right)^2 \frac{1}{V^{\frac{1}{3}}} \tag{48}$$

where S^α and C^α are the area and circumference, respectively, of an ellipse with axes-lengths $d_{m_e^\alpha}$ and $d_{t_e^\alpha}$, while V denotes the volume of the best-fit ellipsoid. S^α can be described as follows:

$$S^\alpha = \frac{\pi}{4}d_{m_e^\alpha}d_{t_e^\alpha}, V = \frac{4}{3}\pi a_1 a_2 a_3 \tag{49}$$

C^α, on the other hand, does not possess a closed-form expression and is instead approximated using an expression proposed by Ramanujan [57] as follows:

$$C^\alpha \approx \frac{\pi}{2}(d_{m_e^\alpha} + d_{t_e^\alpha})\left(1 + \frac{3\,h^2}{10 + \sqrt{4 - 3h^2}}\right), \quad h := \left\|\frac{d_{m_e^\alpha} - d_{t_e^\alpha}}{d_{m_e^\alpha} + d_{t_e^\alpha}}\right\| \qquad (50)$$

The slip system-level grain size for each grain and slip system is computed in a MATLAB script **actual_dist.m**, which is available as part of the PRISMS-Toolbox (See the "Code availability" section). The initial slip resistances are then obtained according to Eq. (11).

4. Modeling fatigue and extreme value statistics

Over the last few decades, crystal plasticity simulations have been employed extensively to investigate the local and extreme value fatigue response of polycrystalline microstructures [49,58–60]. The early stages of fatigue crack formation and growth under high cycle fatigue (HCF) loading conditions are strongly influenced by the local microstructure, including local grain/phase orientation, neighborhood, and morphology [49]. The grain morphology effects considered here may therefore have important implications in the use of these models to predict the extreme value fatigue response and must be evaluated. We employ Fatigue Indicator Parameters (FIPs) as computable quantities of interest within individual grains/subgrain regions [49,61–63]. FIPs serve as surrogate measures of the driving force for fatigue crack formation. Yaghoobi et al. [61] recently presented the open-source PRISMS-Fatigue framework which is employed here to calculate and analyze FIPs. PRISMS-Fatigue is a highly efficient, scalable, flexible, and easy-to-use open-source ICME fatigue framework available to the research community. This work employs a crystallographic version of the Fatemi-Socie FIP [64] introduced by Castelluccio and McDowell [65] defined as

$$FIP_\alpha := \frac{\Delta\gamma_p^\alpha}{2}\left[1 + k\frac{\sigma_n^\alpha}{\sigma_Y}\right] \qquad (51)$$

where $\Delta\gamma_p^\alpha$ is the range of cyclic plastic shear strain on the αth slip system, σ_n^α is the peak stress normal to the slip plane and k controls the influence of σ_n^α which is normalized by the macroscopic yield strength σ_Y [65]. The value of k is set to 10 in accordance with previous work [61–63]. Although the dependence of σ_Y with respect to the three crystallographic textures is computed later, it is held fixed at 517 MPa for all microstructures when comparing FIPs.

FIPs such as FIP_α are commonly employed to examine the fatigue response of polycrystalline microstructure models. In fact, Bozek, Hochhalter, and colleagues [66–68] investigated fatigue incubation life in aluminum alloy 7075-T651 at constituent particles and demonstrated that slip-based metrics computed over appropriate domains could be used to determine which incubated cracks nucleate. Other common FIP formulations include a grain boundary impingement FIP that considers the irreversible plastic shear strain accumulation at

a grain boundary and the stress normal to the grain boundary [69], the accumulated plastic strain energy density [70,71], a combination of the peak hydrostatic stress and maximum local resolved shear stress [72], and stored energy density [73]. In each of these references as well as the current work, FIPs are computed as post-processing operations and do not influence the response or the thermodynamic state of the model. However, recent work has demonstrated the capability to model material degradation directly in the constitutive relations, e.g., Egner et al. [74] related fatigue damage to the third stage of material cyclic softening in a model of P91 steel. In this work, FIPs are computed after 2 fully reversed straining cycles since the local response quickly saturates [63].

FIP_α is calculated at every integration point across the final straining cycle and is subsequently volume averaged to serve two purposes: to alleviate the effects of mesh sensitivity and to reflect the sub-grain fatigue damage process zone over which fatigue crack formation occurs [49]. Several FIP volume averaging strategies exist. The simplest strategy averages FIPs over entire grains but this may too intensely smear the extreme value response in certain parts of a grain. Furthermore, the lognormal grain size distribution results in a non-regularized averaging volume. Castelluccio and McDowell [65] developed a strategy to average FIPs over bands that lie parallel to crystallographic slip planes. Stopka and McDowell [75,76] built on this approach and further separated bands into sub band regions that provide a regularized averaging volume. FIP_α values are volume averaged over these sub-bands in this work and are then fit to an Extreme Value Distribution (EVD) to facilitate rank-ordering of fatigue resistance.

Distributions of a single variable with a sufficiently large sample size n will converge to one of three non-degenerate distributions: 1) Gumbel, 2) Fréchet, and 3) Weibull [77]. FIPs have previously been characterized well by the Gumbel and Fréchet EVDs with a subtle difference depending on whether fully periodic or "thin film" boundary conditions were prescribed [78]. The Weibull EVD requires an upper bound on the data and is therefore not considered here, but PRISMS-Fatigue users have the option to fit FIPs to either the Gumbel or Fréchet EVD [61]. In this work, FIPs are fit to the Gumbel EVD which is expressed as

$$F_{Y_n}(y_n) = \exp\left(-e^{-\alpha_n(y_n - u_n)}\right) \qquad (52)$$

where $F_{Y_n}(y_n)$ is the probability that the value Y_n will be less than or equal to y_n, u_n is the characteristic largest value of the sampled population, and α_n is an inverse measure of the dispersion of the largest value of the population [77]. FIPs are sorted in ascending order with their probabilities estimated by

$$F_{Y_j}(y_j) = \frac{j - 0.3}{n + 0.4} \qquad (53)$$

where j is the rank order of the corresponding FIP and n is the number of FIPs from a single or multiple microstructures. Eq. (53) is written as a linear function of y_n in the form

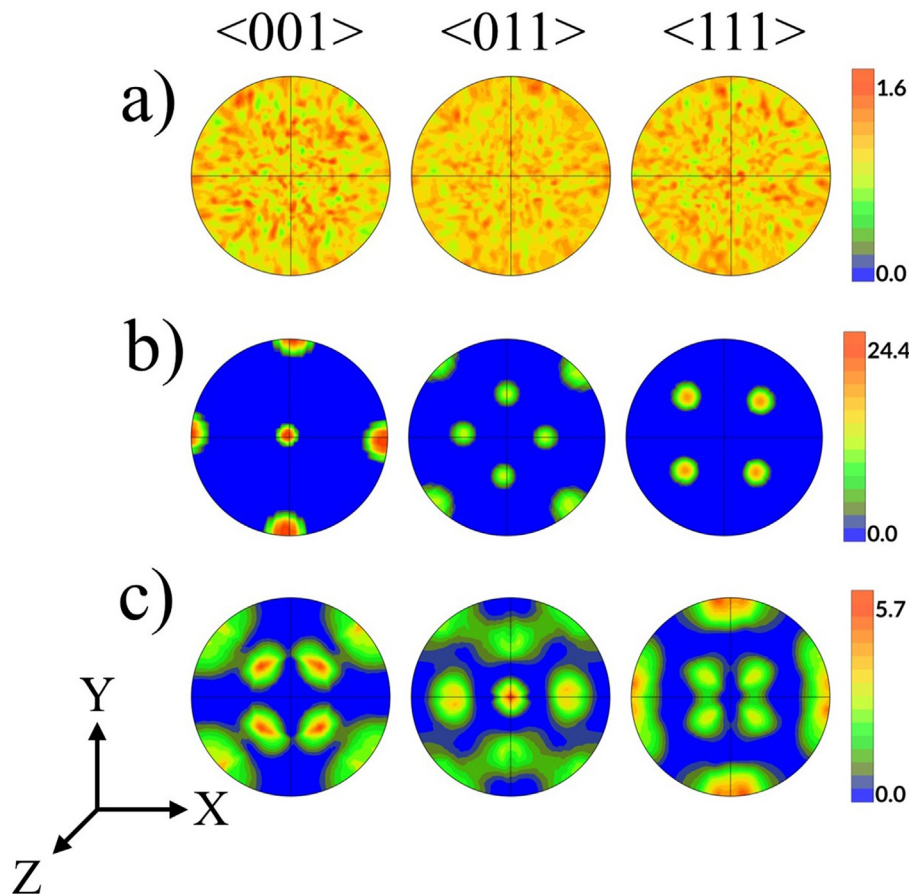$$\ln\left[\ln\left(\frac{1}{F_{Y_n}(y_n)}\right)\right]^{-1} = \alpha_n y_n - \alpha_n u_n \qquad (54)$$

Fig. 1 — Orientation distribution function (ODF) pole figures for the (a) random, (b) cube, and (c) rolled texture.

where α_n is the slope and $-\alpha_n u_n$ is the y-intercept. In this form, data that are well characterized by a Gumbel distribution appear as a straight line. Only a single sub-band volume averaged FIP is considered per grain so that data from multiple elements are not considered. Stopka, Gu, and colleagues [79,80] examined the convergence behavior of FIPs fit to the Gumbel EVD and devised a strategy to predict the maximum FIPs in larger volumes using extreme value theory, which requires rigorous consideration of a FIP threshold in the fitting process. In this work, the highest 100 FIPs from each microstructure are fit to the Gumbel EVD for the sole purpose of rank-ordering relative fatigue resistance. In other words, only the highest FIPs are of interest since these are associated with the highest driving forces for fatigue crack formation.

5.   Results and discussion

5.1.   Simulation details

The developed crystal plasticity framework is implemented within the PRISMS-Plasticity framework [44], a finite element method (FEM) code for solving boundary value problems

arising in continuum and crystal plasticity built on top of the deal.II open-source FEM library [81–83]. In the current work, Al 7075-T6 polycrystalline microstructures with three different crystallographic textures of random, cube, and rolled are generated using DREAM.3D [84], with orientation distribution function (ODF) pole figures shown in Fig. 1(a)–(c). To isolate the effect of grain size from other microstructural features, microstructures from different textures are solely scaled to generate different grain sizes of 25 μm, 50 μm, 200 μm, and 1600 μm. To investigate the effect of grain morphology, microstructures with different textures and average grain size of 50 μm are generated with four aspect ratios, R: 1, 2, 4, 6. An aspect ratio of R implies a relative proportion of R: 1 : 1 of the three axes lengths corresponding to the best-fit ellipsoids used to represent the grains. The proportion R: 1 : 1 with $R \geq 1$ refers to the relative ratio of x: y: z axes lengths. For the rest of this work, the case R = 1 is referred to as 'AR 1' (single quotes removed later when referring to this aspect ratio case), and likewise for the other aspect ratios. Fig. 2 depicts microstructure models with random texture corresponding to AR 1, AR 2, AR 4 and AR 6 where one can observe the grain morphology varying with the aspect ratio R. Each microstructure instantiation is a cube with a structured grid of 100 × 100 × 100 voxels containing approximately 7600 grains.

Four different scenarios are analyzed: (i) random texture with loading along the x direction (ii) cube texture with loading along the x direction (iii) rolled texture with loading along the x direction and (iv) rolled texture with loading along the z direction, all relative to the ODF pole figures shown in Fig. 1. Additionally, we consider cases where microstructures for each aspect ratio are also deformed along the shortest principal axis, i.e., perpendicular to the direction of grain elongation. This is done while ensuring that the texture relative to the loading direction is preserved. For the cube and random textures, the symmetry of the ODF pole figures allows us to simply switch the loading direction from x to z without the need to modify the crystallographic orientations. For the rolled texture however, the orientations are modified to ensure loading along the shortest principal axis, while maintaining texture relative to the loading direction.

For every texture and aspect ratio cases AR 2, AR 4, and AR 6, the corresponding cases with loading along the shortest principal axis are referred to as AR 1/2 (R = 1/2), AR 1/4 (R = 1/4) and AR 1/6 (R = 1/6), respectively. For example, in the case of the cube and random textures loaded along the x direction, AR 1/2 implies loading the microstructure for AR 2 along the z direction. For the rolled texture loaded along the x direction, AR 1/2 implies using the microstructure for AR 2, rotating the crystallographic orientations about the y axis by 90°, and subsequently loading along the z direction. Similarly, for the rolled texture loaded along the z direction, AR 1/2 implies using the microstructure for AR 2, rotating the crystallographic orientations about the y axis by 90°, and subsequently loading along the x direction.

All simulations are performed with periodic boundary conditions implemented into PRISMS-Plasticity following earlier work [78,85], to mimic subsurface material response. In the case of local and extreme value fatigue statistical analysis, cyclic deformation with a strain amplitude of 0.7% is applied to the samples with an average grain size of 50 μm, for the three crystallographic textures, and several grain morphologies.

5.2. Parameter calibration

The room temperature elastic constants for Al 7075-T6 are adopted here [66,86], which are presented in Table 1. The crystal plasticity constitutive parameters are calibrated using

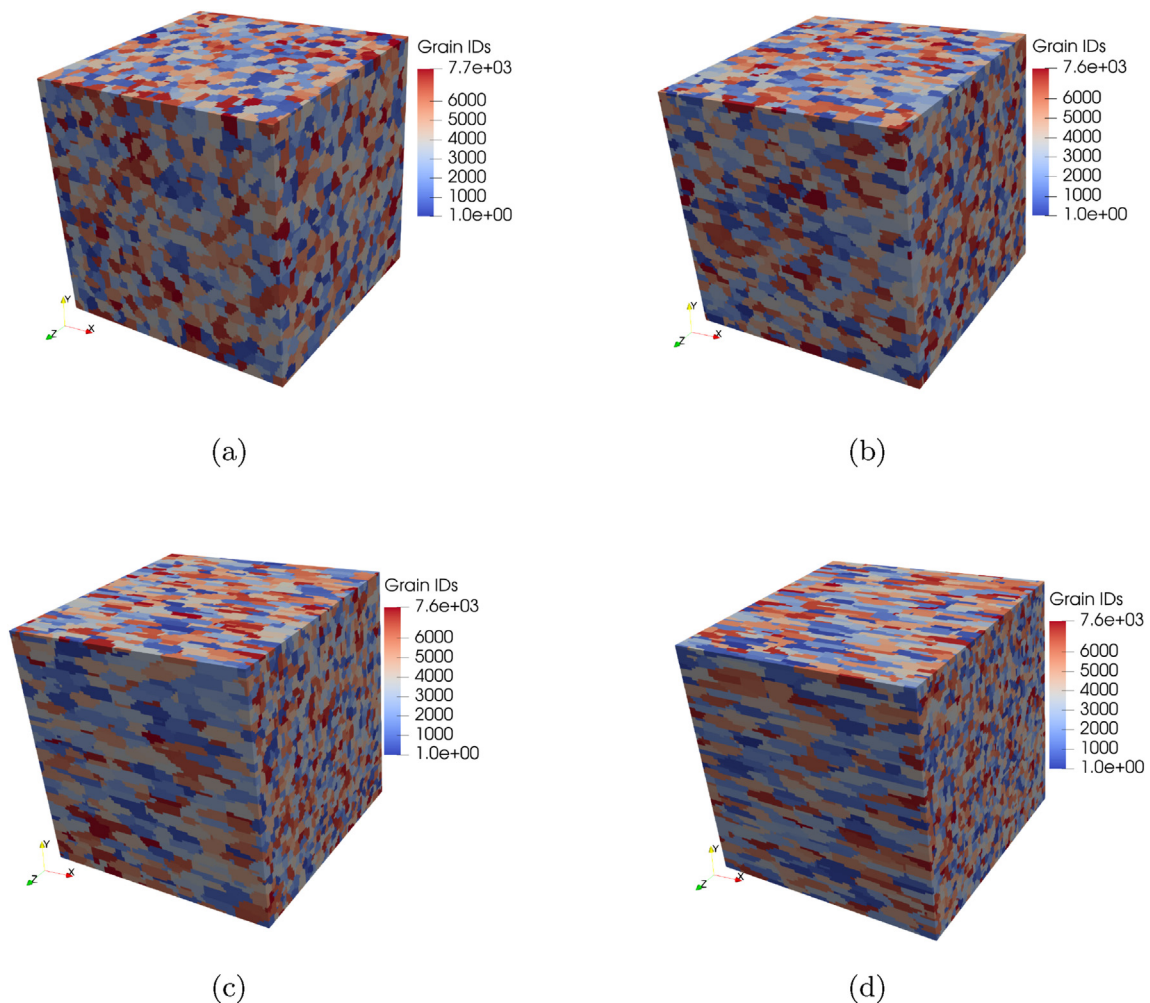(a)   (b)

(c)   (d)

Fig. 2 – Synthetic microstructure models generated using DREAM.3D for four different aspect ratios - (a) AR 1 (equiaxed), (b) AR 2, (c) AR 4, and (d) AR 6.

the experimental results of Al 7075-T6 [87] obtained from cyclic loading tests with strain amplitudes of 1% and 1.8%. To ease the calibration, the Ohno-Wang backstress model described in Eq. (8) is simplified to the Armstrong—Frederick model [88] by assuming just a single backstress contribution with $m_1 = 0$. Isotropic hardening is neglected for all the simulations.

Since FCC polycrystals are modeled in the current work, s_{SI}^α and k^α is assumed to be identical for all slip systems. Accordingly, only two constants should be determined from the calibration procedure, for which two types of simulations are conducted:

1. A periodic cubic microstructure with dimensions 225 μm × 225 μm × 225 μm comprising 100 × 100 × 100 voxels is generated, representative of random texture with approximately 7400 equiaxed grains with a lognormal average grain size of 14 μm. The microstructure is subject to cyclic loading since experimentally measured cyclic stress—strain curves are available for this alloy [87].
2. A periodic microstructure with random texture, an average grain size of 50 μm and approximately 7600 equiaxed grains is generated. The microstructure is then scaled uniformly to different dimensions to mimic three other average grain sizes - 25 μm, 200 μm, and 1600 μm - all of which underwent tensile loading along the x direction.

Strain rate sensitivity exponent of $m = 1/75$ and reference shearing rate of $\dot{\gamma}_0 = 0.0001\ s^{-1}$ are used for the calibration. Displacement-controlled cyclic loading is applied along the x direction using periodic boundary conditions [78,85]. s_{SI}^α and k^α are calibrated to reproduce the Hall-Petch slope of approximately 120 MPa μm$^{1/2}$ for Al 7075-T6 with random texture reported in earlier work [89,90], and the cyclic results reported previously [87]. Additionally, simulations without grain size effect are also performed by setting $k^\alpha = 0$ for which calibrated parameters in previous work [86] are used.

Tables 2 and 3 present the calibrated crystal plasticity constitutive parameters for simulations with and without grain size effects, respectively. Fig. 3(a)—3(b) compare the cyclic responses without the grain size effect using the parameters in Table 2 against the experimental results for strain amplitudes of 1% and 1.8%. Fig. 3(c)—3(d) compare the cyclic responses with the grain size effect using the parameters in Table 3 against the experimental results for strain amplitudes of 1% and 1.8%. Fig. 4 depicts the yield strength variation with average grain size for simulated microstructures with a Hall-Petch slope of approximately $K = 123.7$ MPa μm$^{1/2}$, which is close to the value of 120 MPa μm$^{1/2}$ reported by [89,90].

5.3. Grain size effect

The effects of average grain size on the yield strength of each texture are investigated using samples with equiaxed grains ($R = 1$). The random texture grain size results obtained post

calibration are compared to those of the cube and rolled textures, with average grain sizes of 25 μm, 50 μm, and 200 μm for the two latter textures. Fig. 5(a) depicts the yield strength as a function of average grain size. The variation in yield strength is fit using the expression $\sigma_Y = \sigma_0 + K/\sqrt{d}$, where d is the average grain size and σ_0 and K are the computed Hall-Petch constants shown in Table 4.

The ratio of the maximum and minimum values of σ_0 among the three textures is approximately 1.32. The variability in σ_0 can be explained by considering the distribution of the quantity obtained from the ratio of the global Schmid factor to the normalized slip system-level resistance. For any slip system α in a particular grain, one can compute the global Schmid factor, $\overline{S}^\alpha$, and normalized slip system resistance, $\overline{s}^\alpha$ as

$$\overline{S}^\alpha := |\tilde{\sigma} : S_0^\alpha|; \quad \overline{s}^\alpha := 1 + \frac{k^\alpha}{\sqrt{d_{eff}^\alpha s_{SI}^\alpha}}$$

$$\tilde{\sigma} = \begin{bmatrix} 1 & 0 & 0 \\ 0 & 0 & 0 \\ 0 & 0 & 0 \end{bmatrix} (\text{x loading}), \quad \tilde{\sigma} = \begin{bmatrix} 0 & 0 & 0 \\ 0 & 0 & 0 \\ 0 & 0 & 1 \end{bmatrix} (\text{z loading}) \qquad (55)$$

$$\overline{R}^\alpha := \frac{\overline{S}^\alpha}{\overline{s}^\alpha}$$

where $\overline{R}^\alpha$ is the parameter whose distribution we analyze. This construction is motivated by the ratio of the resolved shear stress to slip resistance appearing in the phenomenological flow rule, Eq. (3), without the backstress term. Fig. 5(b) depicts the distribution of $\overline{R}^\alpha$ for microstructures corresponding to different textures. The probability of larger values (> 0.3) in $\overline{R}^\alpha$ is highest for the cube texture, followed by the rolled (z loading) and random textures being quite similar, and the lowest in rolled (x loading). Since the quantity that we constructed is a measure of ease of crystallographic slip, the yield strength can be directly correlated to the probability of finding higher values of $\overline{R}^\alpha$, and that trend is reflected in Fig. 5(a) in the order of yield strengths for microstructures corresponding to different textures, for a given grain size.

For the Hall-Petch slope K, the ratio of the maximum and minimum values among the textures considered is approximately 1.22. It is interesting to note that for random and rolled (z loading) cases, the values of σ_0 and K are close to each other, suggesting a possible connection between the two. However, as we go in the order of lowest to highest σ_0, K does not depict a monotonic increase. Instead it is the highest at both the ends of the spectrum, i.e, cube and rolled (x loading) cases, and lower for random and rolled (z loading), suggesting a different coupling between texture and the Hall-Petch slope unlike σ_0.

5.4. Grain morphology effect

Synthetic microstructure models are generated with an average grain size of 50 μm and for seven aspect ratios(R) - 1/

Table 1 — Room temperature elastic constants (Units: GPa) of Al 7075-T6 [66].		
C_{11}	C_{12}	C_{44}
107.3	60.9	28.3

Table 2 — Crystal plasticity constitutive parameters for the model without grain size effects [86].			
m	s_{SI}^α(MPa)	h_1(MPa)	r_1
1/75	130	75600	720

Table 3 — Crystal plasticity constitutive parameters for the model with grain size effects.

m	s_{SI}^{α}(MPa)	h_1(MPa)	r_1	k^{α}(MPa $\mu m^{1/2}$)
1/75	35	75600	720	35.5

6, 1/4, 1/2, 1, 2, 4, 6, and the simulated yield strength is depicted in Fig. 6(a). Additionally, for a specific texture (relative to the loading direction) we define the normalized yield strength $\tilde{\sigma}_Y$ as the ratio of the yield strength for a specific aspect ratio R, relative to the yield strength for $R = 1$, for the same texture, as depicted in Fig. 6(b). This figure shows that any deviation from equiaxed grain morphology increases the yield strength. It is important to note that all microstructure models contain the same average number of grains and that grains elongated in one direction shrink in the other two directions, i.e., equiaxed and elongated grains are on average discretized by the same number of elements/voxels. Since the yield strength increases with aspect ratio, this confirms that there is a net decrease in the effective slip system grain size for many grains, resulting in an increase in the slip system resistance (relative to equiaxed grains), in turn

increasing the yield strength. Apart from this common behavior for all texture cases, the yield strength corresponding to the rolled texture (x loading) is more sensitive to aspect ratio than the other textures. Additionally, when the aspect ratio deviates from the equiaxed case, i.e., AR 1, cube texture is the least sensitive, followed by random texture, followed by rolled texture (z loading).

The effect of grain morphology is further investigated using the parameter $\overline{R}^{\alpha}$ defined in Eq. (55). Fig. 7(a)—7(d) depicts the distribution of $\overline{R}^{\alpha}$ for different aspect ratios and textures. As expected, the tails of the distribution towards higher $\overline{R}^{\alpha}$ extend towards larger values as the aspect ratio approaches 1 from either side. It is interesting to note that the slope of the tails of the distribution seems to follow a similar trend (Fig. 7 insets) as the aspect ratios approach 1. In other words, the tail of rolled texture (x loading) approaches 0 much more gradually than the cube texture, which shows the most prominent approach. Among the other two textures, random texture approaches 0 with a higher slope than rolled texture (z loading). This is the reverse order in which the textures are arranged based on their yield strength sensitivity to changes in the aspect ratio close to 1, suggesting a possible correlation
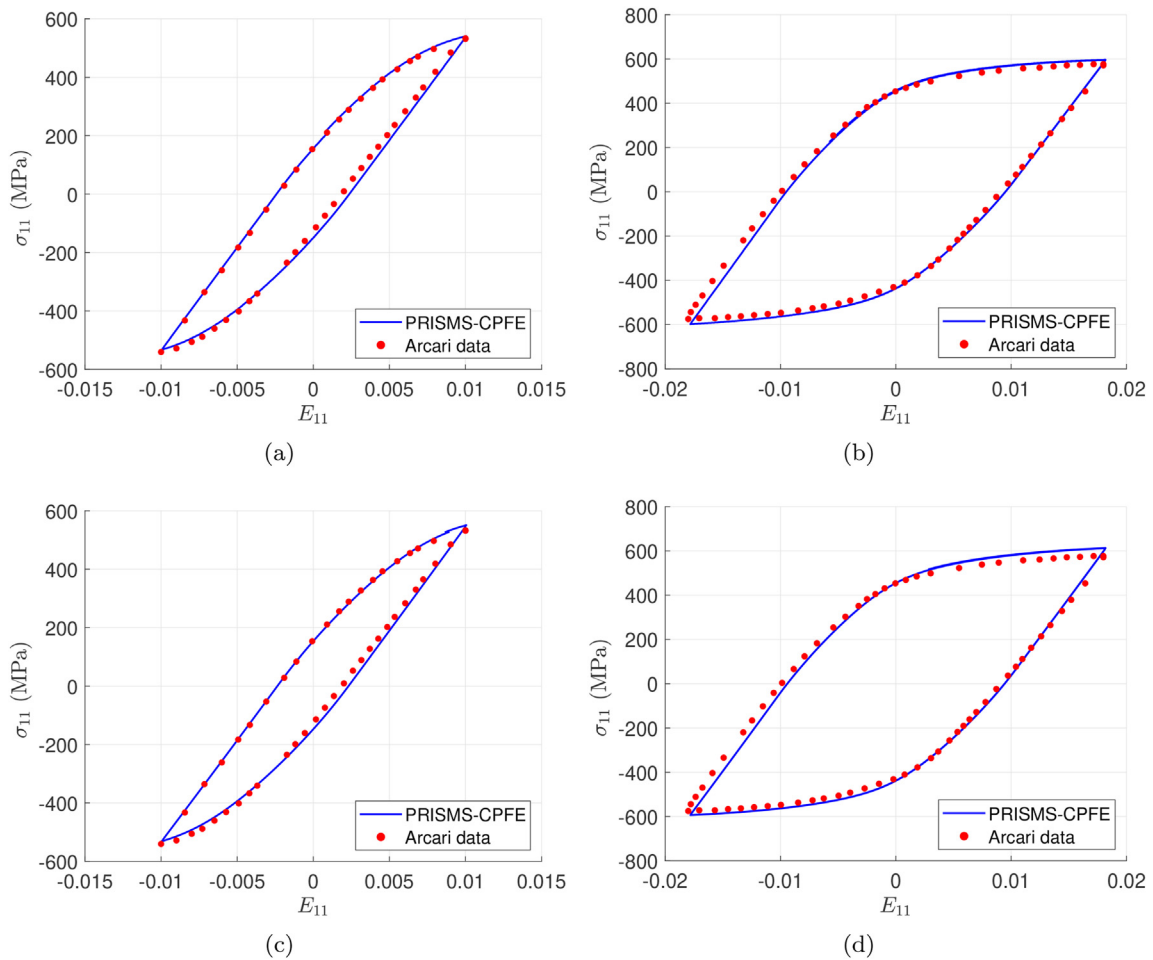

Fig. 3 — Comparison of cyclic stress—strain curves between experiments and simulations. (a) 1% strain amplitude and (b) 1.8% strain amplitude without the grain size effect (c) 1% strain amplitude and (d) 1.8% strain amplitude with the grain size effect.
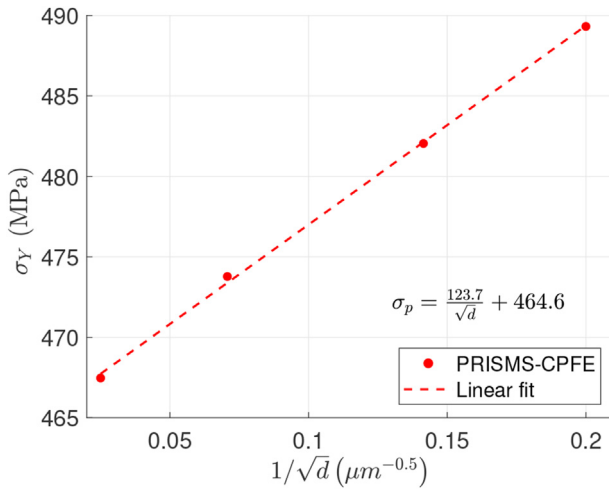
$$\sigma_p = \frac{123.7}{\sqrt{d}} + 464.6$$

Fig. 4 − **Yield strength as a function of average grain size for microstructure models with random texture, used to calibrate the micro Hall−Petch coefficient and Hall-Petch slope of approximately 123.7 MPa $\mu m^{1/2}$.**

Table 4 − Hall-Petch constants for different textures.

Texture	σ_0(MPa)	K(MPa $\mu m^{1/2}$)
Random	464.6	123.7
Cube	384.8	134.4
Rolled(x loading)	506.0	146.1
Rolled(z loading)	473.8	119.3

axes limits to facilitate easy comparisons. The legends and coordinate axes indicate the aspect ratio and straining direction of grains relative to the ODF pole figure, respectively. AR 1 corresponds to the microstructure with equiaxed grains. In contrast, AR 6 and AR 1/6 correspond to grains strained parallel and perpendicular to the direction of grain elongation, respectively. The insets shown in Fig. 8 display the largest values of maximum PSSR.

The histograms from cube textured simulations in Fig. 8(b) show that the maximum of PSSR in cube texture is lower than other textures. Analysis of the cube ODF pole figure in Fig. 1(b) reveals that slip is on average more homogenously distributed in this texture, with 8 of the 12 slip systems accommodating plastic deformation equally. Incorporating of grain size and morphology effects increases the maximum PSSR most notably for grains strained in the direction of grain elongation (AR 6, blue curves), whereas the equiaxed grain morphology shows less change (AR 1, red curves). Histograms for the random texture are shown in Fig. 8(a) with relatively more integration points showing very low or very high plastic slip activity. Each curve resembles a wider distribution as compared to the cube textured data in Fig. 8(b). Grain size and morphology effects do not strongly affect the distributions except in the case of grains strained perpendicular to the direction of grain elongation (AR 1/6, green curves). The equiaxed grain morphology (AR 1, red curves) shows the most plastic slip activity. This data also distinctly overlaps with data from the simulation with grains strained perpendicular to the direction of grain elongation without grain size and morphology effects (AR 1/6, solid green curve) at the highest
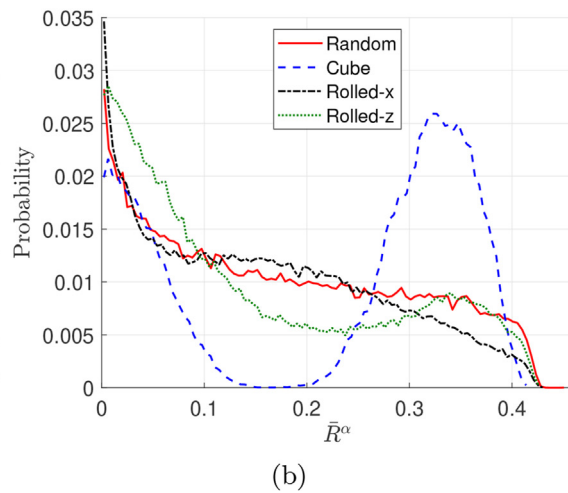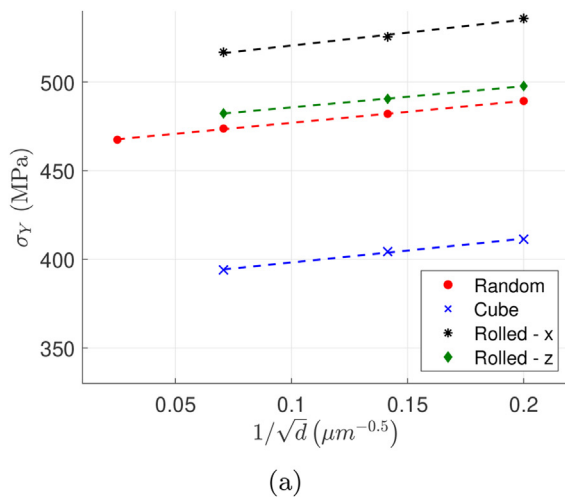
between the nature of the tails of the distribution and the yield strength sensitivity to the aspect ratio.

5.5. *Local maximum plastic shear strain and extreme value fatigue response*

Fig. 8 depicts histograms of the maximum plastic shear strain range (PSSR) at each integration point for each simulation. The PSSR is calculated for each of the 12 slip systems at each integration point using data from the final maximum applied tension and maximum applied compression points in the simulation, and the maximum value at each integration point is then determined. The dotted and solid lines represent simulation data with and without grain size and morphology effects, respectively. All plots in Fig. 8 have the same x and y

(a)

(b)

Fig. 5 − (a) Yield strength as a fuction of average grain size for the random, cube, and rolled textures (x and z loading). The dotted lines denote the best linear fit to the data for the corresponding texture. (b) $\bar{R}^\alpha$ distribution for the microstructure models with different textures and equiaxed grains with average grain size of 50 μm.
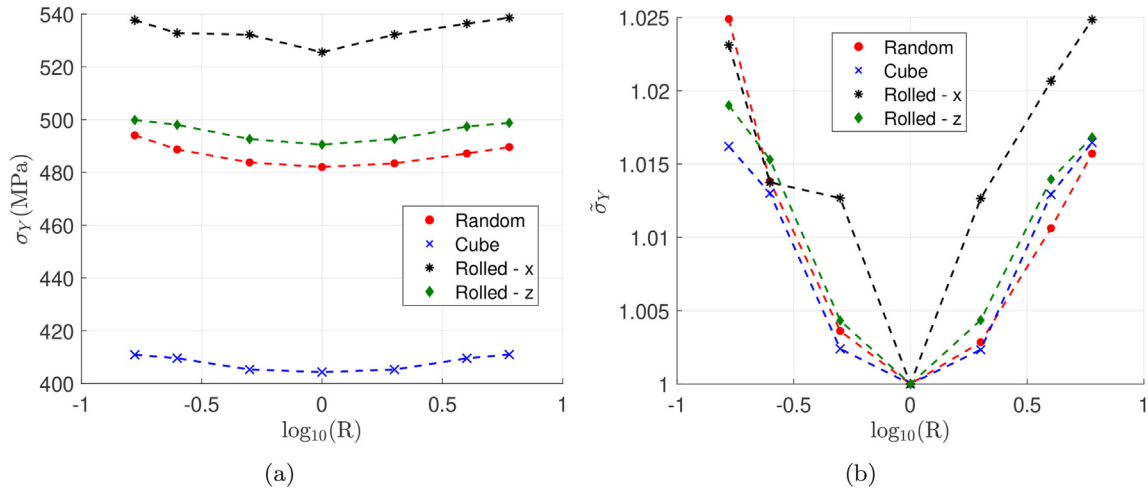
Fig. 6 — (a) Yield strength and (b) normalized yield strength as a function of the four textures and seven grain aspect ratio R in geometric progression from 1/6 to 6, respectively.

values of plastic slip activity, as shown by the inset figure in Fig. 8(a).

Histograms of maximum PSSR for microstructures with rolled crystallographic texture strained in the X and Z directions relative to the ODF pole figure are shown in Fig. 8(c) and Fig. 8(d), respectively. The equiaxed grain morphology once again displays the highest values and almost no influence when grain size and morphology effects are modeled. In
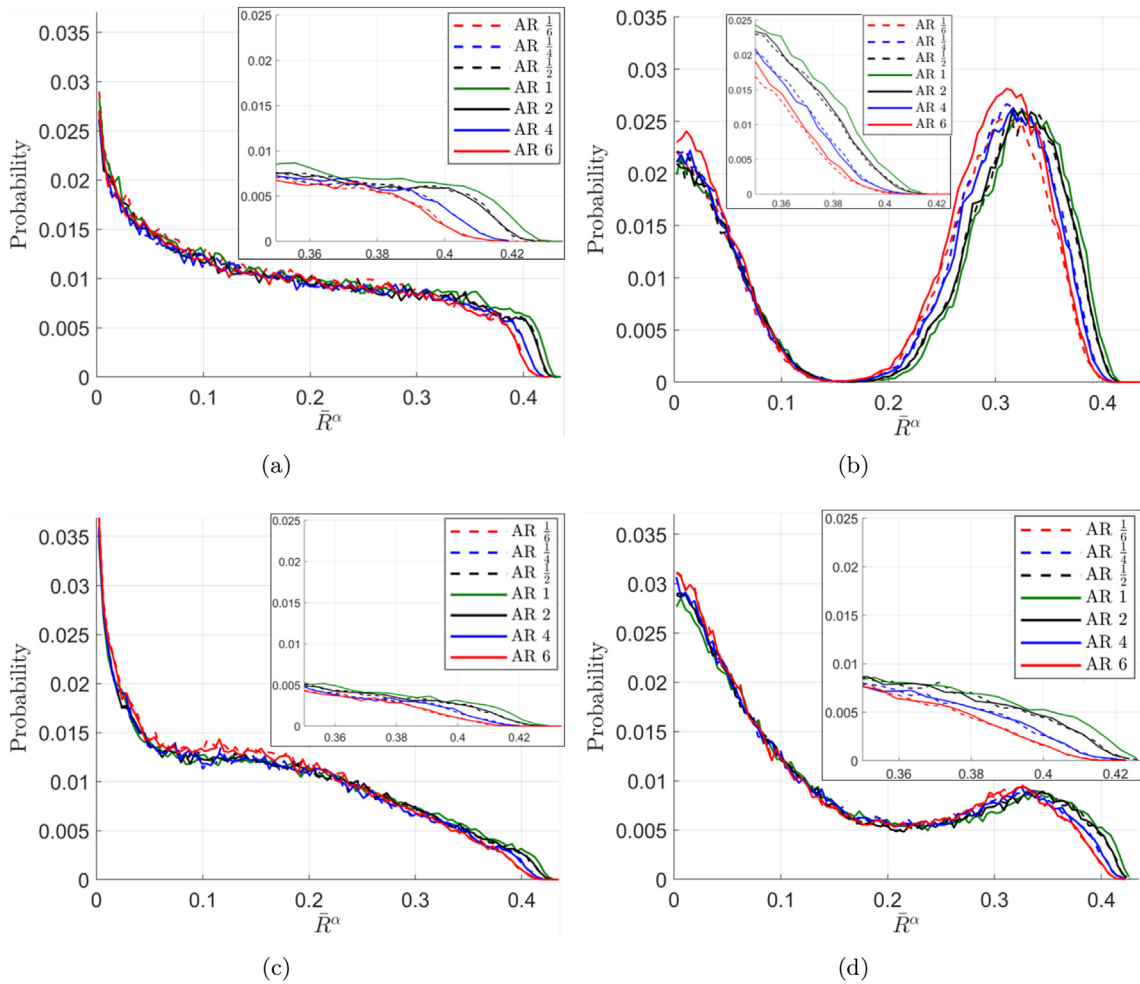

Fig. 7 — Distribution of $\bar{R}^{\alpha}$ for the seven different aspect ratios and for the (a) random texture, (b) cube texture, (c) rolled texture (x loading), and (d) rolled texture (z loading). The insets show the tails of the distributions.
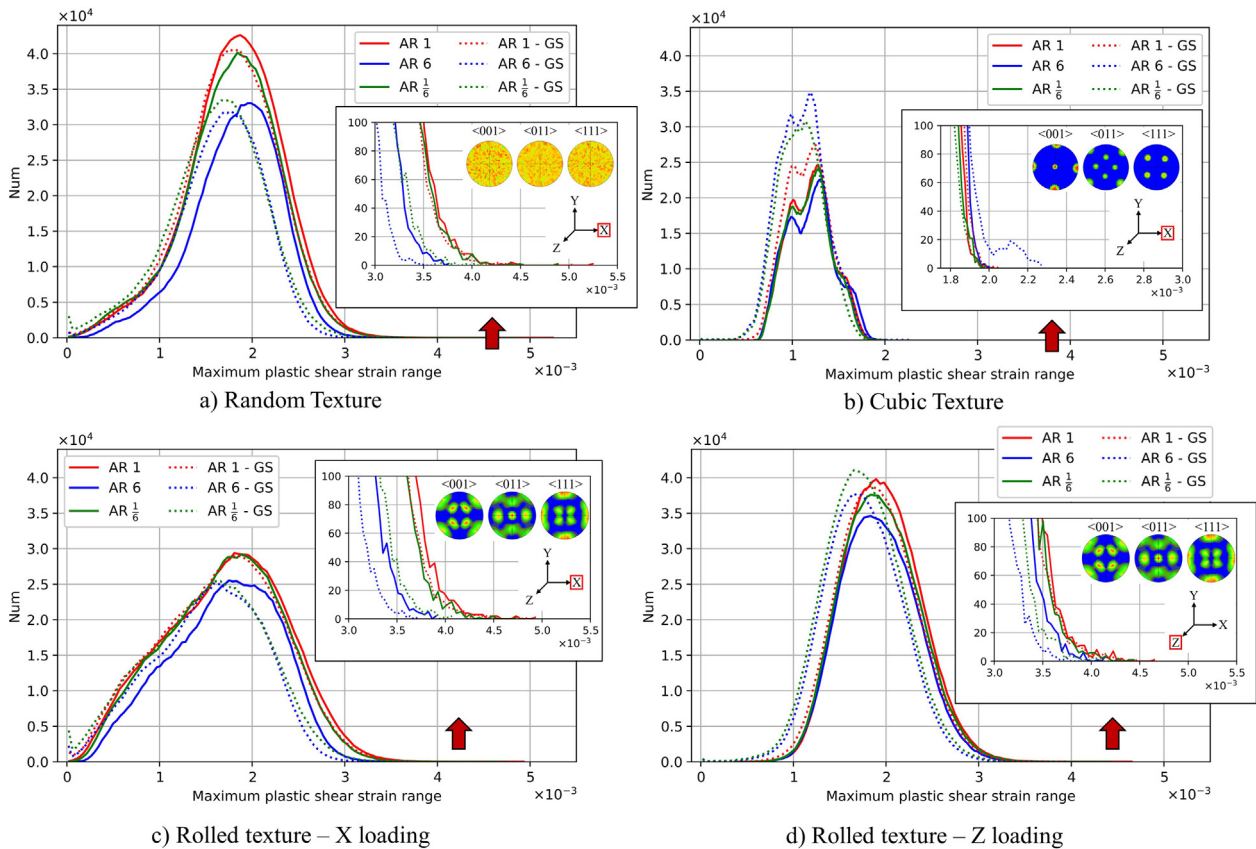
Fig. 8 — Histograms of the maximum plastic shear strain range at each integration point for the (a) random, (b) cube, (c) rolled strained in the X, and (d) rolled strained in the Z crystallographic textures. The straining directions indicated on the coordinate axes are relative to the ODF pole figures. Markers with 'GS' indicate data from simulations that consider grain size and morphology effects.

contrast, the histograms for the AR 6 and AR 1/6 grain morphologies substantially change when grain size and morphology effects are included. Overall, the equiaxed grain morphology displays the largest extreme values of plastic slip (shown in the inset figures in each panel in Fig. 8) except for the cube crystallographic texture.

Fig. 9 shows the highest 100 FIPs from each combination of crystallographic texture and grain aspect ratio fit to the Gumbel EVD, calculated using the crystallographic version of the Fatemi-Socie FIP shown in Eq. (51). The x and y axes limits are once again identical to facilitate easy comparisons. FIPs from the cube textured microstructures are shown in Fig. 9(b) and do not vary significantly between all six data sets. The cube texture in all cases manifests the lowest FIPs and matches previous work by the authors [61,76]. FIPs from microstructures with random crystallographic texture are shown in Fig. 9(a). The equiaxed grain morphology manifests the highest driving forces for fatigue crack formation. Interestingly, when grain size and morphology effects are considered in the model, the extreme value FIPs for the equiaxed grain morphology do not change (red markers). Modeling grain size and morphology effects decreases FIPs only for the elongated grain morphologies, i.e., AR 6 and AR 1/6. FIPs from microstructures with the rolled crystallographic texture are

shown in Fig. 9(c) and Fig. 9(d) for cyclic straining along the x and z directions, respectively. The equiaxed grain morphology once again displays the largest FIPs and lowest sensitivity to the presence of grain size and morphology effects in the model. Similar trends are observed by Stopka and McDowell [76] in that an equiaxed grain morphology reduced FIP magnitudes regardless of crystallographic texture. The unique observation in this work is that any deviation from an equiaxed grain morphology reduces FIPs, which indicates that equiaxed grains represent the "worst case" scenario for the driving forces for fatigue crack formation. It is important to point out that the highest FIPs accord with the highest maximum PSSR shown in Fig. 8, since the computed FIP is based on the PSSR.

For microstructures with equiaxed grain morphology, the changes in the EVD of FIPs are minuscule for all three textures when grain size and morphology effects are included. However, the highest FIPs can considerably change for the random and rolled textures with elongated grain morphology. To further investigate these differences, the microstructures with random and rolled texture are further analyzed. The grains that manifest the highest 10 FIPs are determined with equiaxed grain morphology (i.e., AR 1) and with elongated grains strained perpendicular to the direction of grain
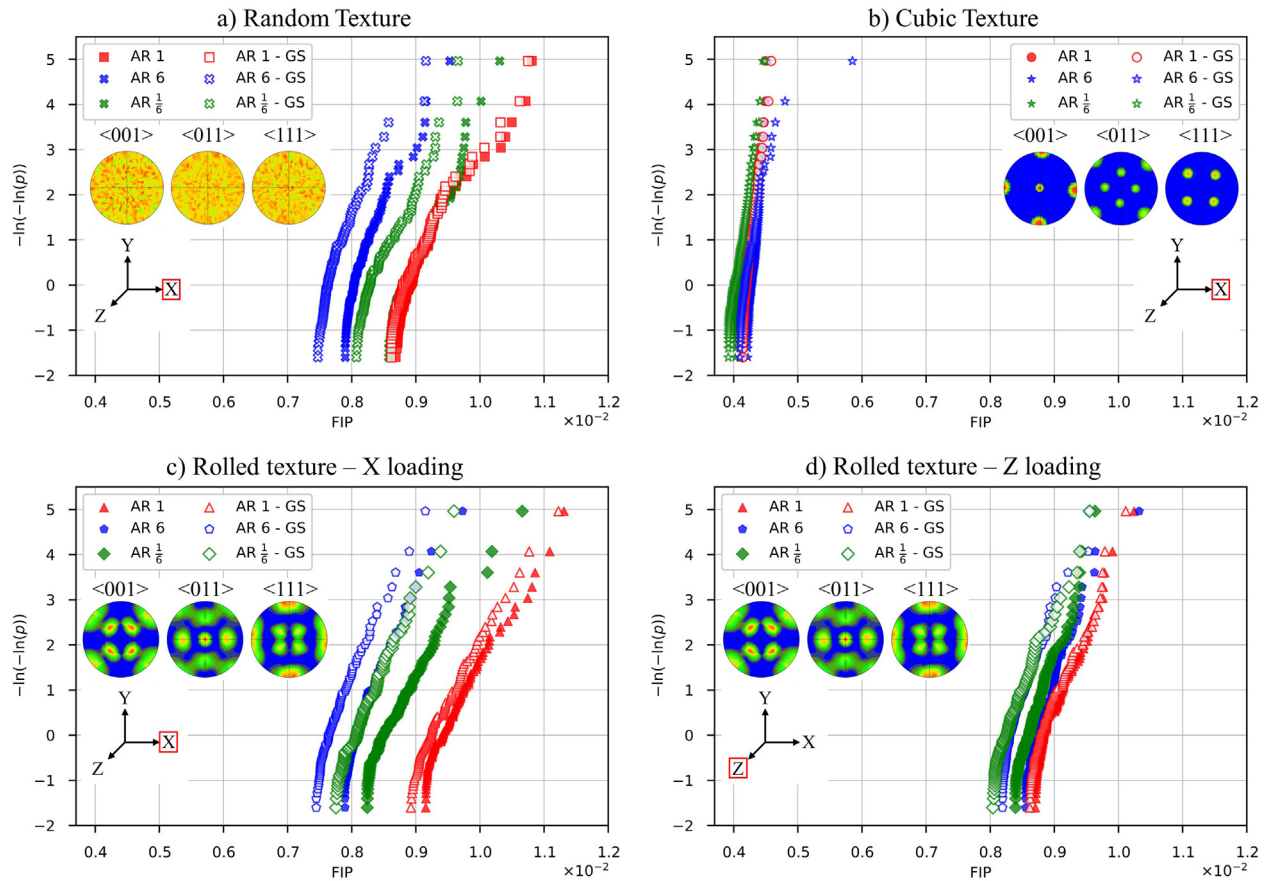
Fig. 9 — The 100 highest sub-band volume averaged Fatigue Indicator Parameters (FIPs) from distinct grains fit to the Gumbel Extreme Value Distribution (EVD) for the a) cube, b) random, c) rolled strained in the X direction, and d) rolled strained in the Z direction crystallographic textures. The straining directions indicated on the coordinate axes are relative to the ODF pole figures. Markers with 'GS' indicate data from simulations that consider grain size and morphology effects.

elongation (i.e., AR 1/6) for both textures. For the random texture with equiaxed grain morphology, 9 out of the 10 highest FIPs occur in the same grain independent of whether the grain size and morphology effects are incorporated into the model. For the rolled texture, this statistic is 7 out of 10 grains that manifest the highest FIPs. For random-textured microstructures with grains strained perpendicular to the direction of grain elongation, only 4 out of the 10 highest FIPs occur in the same grain independent of grain size and morphology effects. For the rolled texture, this statistic is 6 out of the 10 highest FIPs. If the effects of grain size are included without the effects of grain morphology, these important differences would not be observed. These results thus illustrate the importance of including the effect of grain morphology in addition to the grain size effect to accurately capture the extreme value response.

6.   Conclusions

A computational framework is developed to incorporate the effects of grain size and morphology on yield strength and extreme value fatigue response using the crystal plasticity finite element method designed for large scale simulations. A new grain-level length scale is developed for polycrystalline metals and alloys to model the effect of grain size and morphology, which is motivated by the idea of a grain shape factor obtained from discrete dislocation dynamics simulations [21]. Each grain is approximated by its best-fit ellipsoid to extract its length scale which includes both grain size and morphology. The grain-level length scale is then calculated for each slip system and incorporated to define the corresponding slip resistances. The developed framework is available to the community as a part of the open-source software PRISMS-Plasticity and PRISMS-Toolbox.

Simulations of four different texture-loading pairs are performed to study the variation of yield strength with grain size and morphology. A connection is drawn between the distribution of a parameter $\overline{R}^{\alpha}$, whose construction is motivated by the phenomenological flow rule, and the variations in the Hall-Petch constant σ_0, for different textures. Additionally, while there appears to be some correlation between the Hall-Petch slope and σ_0, it does not depict the monotonic behavior relative to different textures as did σ_0.

The model also reflects an increase in yield strength with aspect ratio deviating from equiaxed grains, irrespective of texture. Furthermore, the sensitivity of yield strength to

change in aspect ratio is prominent in the case of rolled texture with loading along the x direction. Additionally, the importance of the tail of the distribution of $\overline{R}^{\alpha}$ is also highlighted in the context of yield strength sensitivity, where the decay characteristics seem to play a role.

Finally, the simulation results demonstrate that incorporating grain size and morphology effects can notably perturb the computed extreme value fatigue response of microstructures, as evaluated using Fatigue Indicator Parameters. Equiaxed grains exhibit the highest driving force for fatigue crack formation. FIPs computed for microstructure models with equiaxed grain morphology are the least sensitive for all three textures with grain size and morphology effects incorporated in the model. However, the highest FIPs can drastically change in the elongated samples for all three textures. This highlights the importance of modeling grain morphology alongside grain size in fatigue analyses. The model presented here can therefore more realistically evaluate the fatigue resistance of polycrystalline microstructures.

Code availability

PRISMS-Plasticity and PRISMS-Fatigue are open-source computer codes available for download at https://github.com/prisms-center/plasticity and https://github.com/prisms-center/Fatigue, respectively. In addition to written tutorials available in the GitHub repositories, a series of video tutorials totaling nearly two and three h of content are available at https://www.youtube.com/playlist?list=PL4yBCojM4Swqy4FRteqxHWSiM1uiOOesj and https://www.youtube.com/playlist?list=PL4yBCojM4Swo3CvlA57syFrzk3p1mugP5, respectively.

The two Python scripts necessary to reproduce the results of this article are available at https://github.com/prisms-center/Fatigue. The MATLAB script used to compute the slip system-level grain size using equivalent ellipsoid information is available at https://github.com/prisms-center/prisms-toolbox/tree/master/PRISMS-Plasticity-Toolbox/Grain_Size_Morphology.

Availability of data and materials

The microstructures, CPFE input files, PRISMS-Plasticity raw simulation results, and individual plots are available on Materials Commons at https://doi.org/10.13011/m3-f90v-gs55.

Declaration of Competing Interest

The authors declare that they have no known competing financial interests or personal relationships that could have appeared to influence the work reported in this paper.

Acknowledgments

REFERENCES

[1] Hall E. The deformation and ageing of mild steel: iii discussion of results. Proc Phys Soc B 1951;64(9):747.

[2] Eshelby J, Frank F, Nabarro F. Xli. the equilibrium of linear arrays of dislocations. The London, Edinburgh, and Dublin Philosophical Magazine and Journal of Science 1951;42(327):351—64.

[3] Petch N. The cleavage strength of polycrystals. Journal of the Iron and Steel Institute 1953;174:25—8.

[4] Cordero ZC, Knight BE, Schuh CA. Six decades of the hall—petch effect—a survey of grain-size strengthening studies on pure metals. Int Mater Rev 2016;61(8):495—512.

[5] G. Voyiadjis, M. Yaghoobi, Size effects in plasticity: from macro to nano, Academic Press.

[6] Schiøtz J, Di Tolla FD, Jacobsen KW. Softening of nanocrystalline metals at very small grain sizes. Nature 1998;391(6667):561—3.

[7] Van Swygenhoven H, Caro A, Farkas D. Grain boundary structure and its influence on plastic deformation of polycrystalline fcc metals at the nanoscale: a molecular dynamics study. Scripta Mater 2001;44(8—9):1513—6.

[8] Van Swygenhoven H, Caro A, Farkas D. A molecular dynamics study of polycrystalline fcc metals at the nanoscale: grain boundary structure and its influence on plastic deformation. Mater Sci Eng, A 2001;309:440—4.

[9] Derlet P, Van Swygenhoven H. Length scale effects in the simulation of deformation properties of nanocrystalline metals. Scripta Mater 2002;47(11):719—24.

[10] Derlet P, Hasnaoui A, Van Swygenhoven H. Atomistic simulations as guidance to experiments. Scripta Mater 2003;49(7):629—35.

[11] Schiøtz J, Jacobsen KW. A maximum in the strength of nanocrystalline copper. Science 2003;301(5638):1357—9.

[12] Hasnaoui A, Derlet P, Van Swygenhoven H. Interaction between dislocations and grain boundaries under an indenter—a molecular dynamics simulation. Acta Mater 2004;52(8):2251—8.

[13] Wolf D, Yamakov V, Phillpot S, Mukherjee A, Gleiter H. Deformation of nanocrystalline materials by molecular-dynamics simulation: relationship to experiments? Acta Mater 2005;53(1):1—40.

[14] Voyiadjis GZ, Yaghoobi M. Role of grain boundary on the sources of size effects. Comput Mater Sci 2016;117:315—29.

[15] Voyiadjis GZ, Yaghoobi M. Review of nanoindentation size effect: experiments and atomistic simulation. Crystals 2017;7(10):321.

[16] Voyiadjis G, Yaghoobi M. Size effects during nanoindentation: molecular dynamics simulation. In: Handbook of nonlocal continuum mechanics for materials and structures. Cham, Switzerland: Springer International Publishing AG; 2019. p. 39—76.

[17] Biner S, Morris J. A two-dimensional discrete dislocation simulation of the effect of grain size on

strengthening behaviour. Model Simulat Mater Sci Eng 2002;10(6):617.

[18] Lefebvre S, Devincre B, Hoc T. Yield stress strengthening in ultrafine-grained metals: a two-dimensional simulation of dislocation dynamics. J Mech Phys Solid 2007;55(4):788—802.

[19] Ohashi T, Kawamukai M, Zbib H. A multiscale approach for modeling scale-dependent yield stress in polycrystalline metals. Int J Plast 2007;23(5):897—914.

[20] Zhang X, Aifantis KE, Senger J, Weygand D, Zaiser M. Internal length scale and grain boundary yield strength in gradient models of polycrystal plasticity: how do they relate to the dislocation microstructure? J Mater Res 2014;29(18):2116—28.

[21] Jiang M, Devincre B, Monnet G. Effects of the grain size and shape on the flow stress: a dislocation dynamics study. Int J Plast 2019;113:111—24.

[22] Acharya A, Beaudoin AJ. Grain-size effect in viscoplastic polycrystals at moderate strains. J Mech Phys Solid 2000;48(10):2213—30.

[23] Evers L, Parks D, Brekelmans W, Geers M. Crystal plasticity model with enhanced hardening by geometrically necessary dislocation accumulation. J Mech Phys Solid 2002;50(11):2403—24.

[24] Cheong K, Busso E, Arsenlis A. A study of microstructural length scale effects on the behaviour of fcc polycrystals using strain gradient concepts. Int J Plast 2005;21(9):1797—814.

[25] Bayley C, Brekelmans W, Geers M. A three-dimensional dislocation field crystal plasticity approach applied to miniaturized structures. Phil Mag 2007;87(8—9):1361—78.

[26] Shenoy M, Tjiptowidjojo Y, McDowell D. Microstructure-sensitive modeling of polycrystalline in 100. Int J Plast 2008;24(10):1694—730.

[27] Bargmann S, Ekh M, Runesson K, Svensden B. Modeling of polycrystals with gradient crystal plasticity: a comparison of strategies. Phil Mag 2010;90(10):1263—88.

[28] Lim H, Lee M, Kim J, Adams B, Wagoner R. Simulation of polycrystal deformation with grain and grain boundary effects. Int J Plast 2011;27(9):1328—54.

[29] Sun S, Sundararaghavan V. A probabilistic crystal plasticity model for modeling grain shape effects based on slip geometry. Acta Mater 2012;60(13—14):5233—44.

[30] Lim H, Subedi S, Dt F, Bl A, Rh W. A practical meso-scale polycrystal model to predict dislocation densities and the hall—petch effect. Mater Trans 2014;55(1):35—8.

[31] Haouala S, Segurado J, LLorca J. An analysis of the influence of grain size on the strength of fcc polycrystals by means of computational homogenization. Acta Mater 2018;148:72—85.

[32] Fleck N, Muller G, Ashby MF, Hutchinson JW. Strain gradient plasticity: theory and experiment. Acta Metall Mater 1994;42(2):475—87.

[33] Hutchinson J, Fleck N. Strain gradient plasticity. Adv Appl Mech 1997;33:295—361.

[34] Voyiadjis GZ, Al-Rub RKA. Gradient plasticity theory with a variable length scale parameter. Int J Solid Struct 2005;42(14):3998—4029.

[35] Al-Rub RKA, Voyiadjis GZ. A physically based gradient plasticity theory. Int J Plast 2006;22(4):654—84.

[36] Cruzado A, Lucarini S, LLorca J, Segurado J. Crystal plasticity simulation of the effect of grain size on the fatigue behavior of polycrystalline inconel 718. Int J Fatig 2018;113:236—45.

[37] Fromm BS, Adams BL, Ahmadi S, Knezevic M. Grain size and orientation distributions: application to yielding of α-titanium. Acta Mater 2009;57(8):2339—48.

[38] Bunge H, Wagner F, Van Houtte P. A new way to include the grain shape in texture simulations with the taylor model. J Phys, Lett 1985;46(23):1109—13.

[39] Tiem S, Berveiller M, Canova G. Grain shape effects on the slip system activity and on the lattice rotations. Acta Metall 1986;34(11):2139—49.

[40] Wagner F, Bunge H, Van Houtte P. Influence of grain size and shape on the texture formation and the anisotropy coefficient. In: ICOTOM: eighth international conference on textures of materials; 1987. p. 369—74.

[41] Taylor GI. Plastic strain in metals. J Inst Met 1938;62:307—24.

[42] Delannay L, Melchior M, Signorelli J, Remacle J-F, Kuwabara T. Influence of grain shape on the planar anisotropy of rolled steel sheets — evaluation of three models. Comput Mater Sci 2009;45(3):739—43.

[43] Delannay L, Barnett MR. Modelling the combined effect of grain size and grain shape on plastic anisotropy of metals. Int J Plast 2012;32:70—84.

[44] Yaghoobi M, Ganesan S, Sundar S, Lakshmanan A, Rudraraju S, Allison JE, et al. Prisms-plasticity: an open-source crystal plasticity finite element software. Comput Mater Sci 2019;169:109078.

[45] Yaghoobi M, Allison JE, Sundararaghavan V. Multiscale modeling of twinning and detwinning behavior of hcp polycrystals. Int J Plast 2020;127:102653.

[46] Ganesan S, Yaghoobi M, Githens A, Chen Z, Daly S, Allison JE, et al. The effects of heat treatment on the response of we43 mg alloy: crystal plasticity finite element simulation and sem-dic experiment. Int J Plast 2021;137:102917.

[47] Yaghoobi M, Chen Z, Murphy-Leonard AD, Sundararaghavan V, Daly S, Allison JE. Deformation twinning and detwinning in extruded mg-4al: in-situ experiment and crystal plasticity simulation. Int J Plast 2022;155:103345.

[48] Yaghoobi M, Allison JE, Sundararaghavan V. Prisms-plasticity tm: an open-source rapid texture evolution analysis pipeline, Integrating Materials and Manufacturing Innovation, [in revision], 2022.

[49] McDowell D, Dunne F. Microstructure-sensitive computational modeling of fatigue crack formation. Int J Fatig 2010;32(9):1521—42.

[50] Kröner E. Allgemeine kontinuumstheorie der versetzungen und eigenspannungen. Arch Ration Mech Anal 1959;4(1):273.

[51] Lee EH. Elastic-plastic deformation at finite strains. J Appl Mech 1969;36:1—6.

[52] Asaro RJ, Needleman A. Overview no. 42 texture development and strain hardening in rate dependent polycrystals. Acta Metall 1985;33(6):923—53.

[53] Anand L. Constitutive equations for hot-working of metals. Int J Plast 1985;1(3):213—31.

[54] Kalidindi SR, Bronkhorst CA, Anand L. Crystallographic texture evolution in bulk deformation processing of fcc metals. J Mech Phys Solid 1992;40(3):537—69.

[55] Ohno N, Wang J-D. Kinematic hardening rules with critical state of dynamic recovery, part i: formulation and basic features for ratchetting behavior. Int J Plast 1993;9(3):375—90.

[56] McDowell D. Stress state dependence of cyclic ratchetting behavior of two rail steels. Int J Plast 1995;11(4):397—421.

[57] Ramanujan S. Modular equations and approximations to π. Q J Math 1914;45:350—72.

[58] Dunne F. Fatigue crack nucleation: mechanistic modelling across the length scales. Curr Opin Solid State Mater Sci 2014;18(4):170—9 [slip Localization and Transfer in Deformation and Fatigue of Polycrystals].

[59] Sangid MD. The physics of fatigue crack initiation. Int J Fatig 2013;57:58—72.

[60] Jirandehi AP, Khonsari MM. General quantification of fatigue damage with provision for microstructure: a review. Fatig Fract Eng Mater Struct 2021;44(8):1973—99.

[61] Yaghoobi M, Stopka KS, Lakshmanan A, Sundararaghavan V, Allison JE, McDowell DL. Prisms-fatigue computational framework for fatigue analysis in polycrystalline metals and alloys. npj Computational Materials 2021;7(1):1–12.

[62] Stopka KS, Yaghoobi M, Allison JE, McDowell DL. Effects of boundary conditions on microstructure-sensitive fatigue crystal plasticity analysis. Integrating Materials and Manufacturing Innovation 2021;10:393–412.

[63] Stopka KS, Yaghoobi M, Allison JE, McDowell DL. Simulated effects of sample size and grain neighborhood on the modeling of extreme value fatigue response. Acta Mater 2022;224:117524.

[64] Fatemi A, Socie DF. A critical plane approach to multiaxial fatigue damage including out-of-phase loading. Fatig Fract Eng Mater Struct 1988;11(3):149–65.

[65] Castelluccio GM, McDowell DL. Assessment of small fatigue crack growth driving forces in single crystals with and without slip bands. Int J Fract 2012;176(1):49–64.

[66] Bozek J, Hochhalter J, Veilleux M, Liu M, Heber G, Sintay S, et al. A geometric approach to modeling microstructurally small fatigue crack formation: I. probabilistic simulation of constituent particle cracking in aa 7075-t651. Model Simulat Mater Sci Eng 2008;16(6):065007.

[67] Hochhalter JD, Littlewood DJ, Christ RJ, Veilleux MG, Bozek JE, Ingraffea AR, et al. A geometric approach to modeling microstructurally small fatigue crack formation: II. physically based modeling of microstructure-dependent slip localization and actuation of the crack nucleation mechanism in AA 7075-t651. Model Simulat Mater Sci Eng 2010;18(4):045004.

[68] Hochhalter JD, Littlewood DJ, Veilleux MG, Bozek JE, Maniatty AM, Rollett AD, et al. A geometric approach to modeling microstructurally small fatigue crack formation: III. development of a semi-empirical model for nucleation. Model Simulat Mater Sci Eng 2011;19(3):035008.

[69] Smith BD, Shih DS, McDowell DL. Fatigue hot spot simulation for two widmanstätten titanium microstructures. Int J Fatig 2016;92:116–29.

[70] Prithivirajan V, Sangid MD. Examining metrics for fatigue life predictions of additively manufactured in718 via crystal plasticity modeling including the role of simulation volume and microstructural constraints. Mater Sci Eng, A 2020;783:139312.

[71] Bandyopadhyay R, Sangid MD. A probabilistic fatigue framework to enable location-specific lifing for critical thermo-mechanical engineering applications. Integrating Materials and Manufacturing Innovation 2021;10(1):20–43.

[72] Hallberg H, Ås SK, Skallerud B. Crystal plasticity modeling of microstructure influence on fatigue crack initiation in extruded al6082-t6 with surface irregularities. Int J Fatig 2018;111:16–32.

[73] Cao M, Liu Y, Dunne FP. A crystal plasticity approach to understand fatigue response with respect to pores in additive manufactured aluminium alloys. Int J Fatig 2022;161:106917.

[74] Egner W, Sulich P, Mroziński S, Egner H. Modelling thermo-mechanical cyclic behavior of p91 steel. Int J Plast 2020;135:102820.

[75] Stopka KS, McDowell DL. Microstructure-sensitive computational multiaxial fatigue of al 7075-t6 and duplex ti-6al-4v. Int J Fatig 2020;133:105460.

[76] Stopka KS, McDowell DL. Microstructure-sensitive computational estimates of driving forces for surface versus subsurface fatigue crack formation in duplex ti-6al-4v and al 7075-t6. JOM 2020;72(1):28–38.

[77] Castillo E. Extreme value theory in engineering. Elsevier; 2012.

[78] Przybyla CP, McDowell DL. Microstructure-sensitive extreme value probabilities for high cycle fatigue of ni-base superalloy in100. Int J Plast 2010;26(3):372–94.

[79] Stopka KS, Gu T, McDowell DL. Effects of algorithmic simulation parameters on the prediction of extreme value fatigue indicator parameters in duplex ti-6al-4v. Int J Fatig 2020;141:105865.

[80] Gu T, Stopka KS, Xu C, McDowell DL. Prediction of maximum fatigue indicator parameters for duplex ti–6al–4v using extreme value theory. Acta Mater 2020;188:504–16.

[81] Arndt D, Bangerth W, Blais B, Clevenger TC, Fehling M, Grayver AV, et al. The deal.II library, version 9.2. J Numer Math 2020;28(3):131–46.

[82] Arndt D, Bangerth W, Davydov D, Heister T, Heltai L, Kronbichler M, et al. The deal.II finite element library: design, features, and insights. Comput Math Appl 2021;81:407–22.

[83] Bangerth W, Hartmann R, Kanschat G. deal.II — a general purpose object oriented finite element library. ACM Trans Math Software 2007;33(4):24/1–24/27.

[84] Groeber MA, Jackson MA. Dream. 3d: a digital representation environment for the analysis of microstructure in 3d. Integrating materials and manufacturing innovation 2014;3(1):56–72.

[85] Przybyla CP. Microstructure-sensitive extreme value probabilities of fatigue in advanced engineering alloys. Georgia Institute of Technology; 2010.

[86] Hennessey C, Castelluccio GM, McDowell DL. Sensitivity of polycrystal plasticity to slip system kinematic hardening laws for al 7075-t6. Mater Sci Eng, A 2017;687:241–8.

[87] Arcari A. Enhanced strain-based fatigue methodology for high strength aluminum alloys. Ph.D. thesis. Virginia Tech; 2010.

[88] Armstrong PJ, Frederick C. A mathematical representation of the multiaxial Bauschinger effect, vol. 731. Central Electricity Generating Board [and] Berkeley Nuclear Laboratories; 1966.

[89] Wert J. In: Gifkins RC, editor. Strength of metal alloys; 1980.

[90] Shaeri M, Shaeri M, Ebrahimi M, Salehi M, Seyyedein S. Effect of ecap temperature on microstructure and mechanical properties of al–zn–mg–cu alloy. Prog Nat Sci: Mater Int 2016;26(2):182–91.